

Regulatory imbalance between LRRK2 kinase, PPM1H phosphatase, and ARF6 GTPase disrupts the axonal transport of autophagosomes

Dan Dou^{1,2,3}, Erin M. Smith¹, Chantell S. Evans⁴, C. Alexander Boecker^{5,6}, Erika L.F. Holzbaur^{1,2,3,6}

Affiliations: ¹Department of Physiology, Perelman School of Medicine, University of Pennsylvania, Philadelphia, PA 19104, USA; ²Aligning Science Across Parkinson's (ASAP) Collaborative Research Network, Chevy Chase, MD, USA; ³Neuroscience Graduate Group, University of Pennsylvania Perelman School of Medicine, Philadelphia, PA, USA; ⁴Duke University Medical Center, Duke University, Durham, NC 27710, USA; ⁵Department of Neurology, University Medical Center Goettingen, 37077 Goettingen, Germany

Footnotes: ⁶Authors contributed equally to this work

Correspondence: alexander.boecker@med.uni-goettingen.de, holzbaur@pennmedicine.upenn.edu

ORCID IDs:

D.D. 0000-0002-6939-4752

C.S.E. 0000-0001-9401-8604

C.A.B. 0000-0001-9701-5273

E.L.F.H. 0000-0001-5389-4114

SUMMARY

Gain-of-function mutations in the *LRRK2* gene cause Parkinson's disease (PD), increasing phosphorylation of RAB GTPases through hyperactive kinase activity. We found that LRRK2-hyperphosphorylated RABs disrupt the axonal transport of autophagosomes by perturbing the coordinated regulation of cytoplasmic dynein and kinesin motors. In iPSC-derived human neurons, knock-in of the strongly-hyperactive *LRRK2*-p.R1441H mutation caused striking impairments in autophagosome transport, inducing frequent directional reversals and pauses. Knock-out of the opposing Protein Phosphatase 1H (PPM1H) phenocopied the effect of hyperactive LRRK2. Overexpression of ADP-ribosylation factor 6 (ARF6), a GTPase that acts as a switch for selective activation of dynein or kinesin, attenuated transport defects in both p.R1441H knock-in and PPM1H knock-out neurons. Together, these findings support a model where a regulatory imbalance between LRRK2-hyperphosphorylated RABs and ARF6 induces an unproductive “tug-of-war” between dynein and kinesin, disrupting processive autophagosome transport. This disruption may contribute to PD pathogenesis by impairing the essential homeostatic functions of axonal autophagy.

Keywords: LRRK2, PPM1H, RAB GTPases, ARF6, autophagy, axonal transport, Parkinson's disease

INTRODUCTION

The leucine-rich repeat kinase 2 (*LRRK2*) gene is a prominent pleomorphic risk locus for Parkinson's disease (PD), a devastating neurodegenerative disease with debilitating motor and non-motor symptoms. Autosomal dominant missense mutations in *LRRK2* are the most common genetic cause of PD, accounting for ~5% of familial forms (Healy et al., 2008). In addition, genome-wide association studies have linked noncoding variants in *LRRK2* to risk of sporadic PD.

LRRK2 is a large, multidomain enzyme that includes both a Roc-COR tandem GTPase domain and a catalytic kinase domain. Seven gain-of-function pathogenic mutations either directly (mutations located in the kinase domain) or indirectly (mutations located in the Roc or COR domains) increase *LRRK2* kinase activity. The most common pathogenic mutation is *LRRK2*-p.G2019S, located in the kinase domain. Three Roc domain mutations at the p.R1441 hotspot (p.R1441C/G/H) decrease *LRRK2* GTPase activity and hyperactivate kinase activity to a similar extent (Steger et al., 2016; Wu et al., 2019). All three mutations induce higher levels of kinase hyperactivity than p.G2019S (Kalogeropoulou et al., 2022; Steger et al., 2016). p.R1441 hotspot mutations may also be more highly penetrant than p.G2019S (Haugarvoll et al., 2008; Klein and Westenberger, 2012).

LRRK2 phosphorylates a subset of RAB GTPases (RABs) that coordinate intracellular vesicle trafficking by selectively recruiting effector proteins. Protein Phosphatase 1H (PPM1H) has recently been found to counteract *LRRK2* activity by specifically dephosphorylating *LRRK2*-phosphorylated RAB GTPases (Berndsen et al., 2019). Hyperactive *LRRK2* mutations induce increased phosphorylation of RABs, altering their interactions with downstream binding partners. These binding partners include the motor adaptor proteins JNK-interacting protein 3 and 4 (JIP3/4), which selectively interact with *LRRK2*-phosphorylated RAB proteins and control activation of the molecular motors kinesin and dynein (Bonet-Ponce et al., 2020; Kluss et al., 2022; Waschbüsch et al., 2020). Altered binding to effector proteins induced by *LRRK2*-mediated phosphorylation of RABs is predicted to alter RAB-dependent intracellular vesicle transport. In recent work, we found that *LRRK2*-p.G2019S decreases the processivity of retrograde axonal AV transport by recruiting JIP4 and inducing inappropriate kinesin activity (Boecker and Holzbaur, 2021; Boecker et al., 2021).

The transport of autophagic vesicles (AVs) in neurons is of particular importance for the maintenance of axonal homeostasis. AVs are formed in the distal axon and at presynaptic sites before undergoing processive retrograde motility toward the soma, driven primarily by the microtubule-associated motor protein cytoplasmic dynein (Cheng et al., 2015; Maday and Holzbaur, 2014; Maday et al., 2012; Neisch et al., 2017; Stavoe et al., 2016). The opposing motor kinesin remains bound to AVs during dynein-driven transport but is auto-inhibited under normal conditions (Boecker et al., 2021; Fu and Holzbaur, 2014; Maday et al., 2012). During retrograde transport, the AV fuses with 1-2 lysosomes, lowering the intra-

luminal pH and activating degradative enzymes (Cason et al., 2022). Importantly, the transport of AVs is tightly-linked to AV maturation and function in cargo degradation (Cason and Holzbaur, 2022; Cason et al., 2021; Wong and Holzbaur, 2014).

Here, we demonstrate that the opposing activities of LRRK2 kinase and PPM1H phosphatase dictate an important regulatory balance for the motor proteins that drive autophagosome transport. We found that neurons expressing the highly-hyperactive *LRRK2*-p.R1441H mutation exhibited a more severe transport deficit than was previously observed in p.G2019S knock-in (KI) neurons (Boecker et al., 2021), suggesting that increased disruptions in autophagosome transport scale with higher levels of LRRK2 kinase activity. In complementary experiments, we found that knock-out (KO) of PPM1H also impaired AV transport, while PPM1H overexpression rescued AV transport in p.G2019S KI neurons, confirming the model that balanced kinase and phosphatase activities are required for normal autophagosome transport. Finally, we found that overexpression of ADP-ribosylation factor 6 (ARF6), which acts as a switch to regulate the association of the activating adaptor JIP3/4 with either dynein/dynactin or kinesin (Montagnac et al., 2009), attenuated defective AV transport in both p.R1441H KI and PPM1H KO neurons. Thus, our data indicate that the balanced interplay among ARF6 activity, JIP3/4 association, and RAB phosphorylation state permits unopposed retrograde autophagosome transport in WT conditions, while hyperactivation of LRRK2 by PD-associated mutations leads to a regulatory imbalance, resulting in an inappropriate “tug-of-war” between dynein and kinesin. Our data robustly link hyperphosphorylation of RABs to defects in neuronal autophagy, an essential homeostatic pathway that has long been implicated in PD pathogenesis.

RESULTS

Endogenous LRRK2-p.R1441H disrupts the axonal transport of autophagosomes in iPSC-derived neurons.

A point mutation in the kinase domain of LRRK2 (*LRRK2*-p.G2019S) disrupts the axonal transport of autophagic vesicles (AVs) in mammalian neurons. Mutations in the p.R1441 hotspot located in the ROC domain of LRRK2 also cause PD, potentially with higher penetrance (Domingo and Klein, 2018; Haugarvoll et al., 2008; Ruiz-Martínez et al., 2010). Consistent with previous reports, we found that *LRRK2*-p.R1441C causes a higher magnitude of kinase hyperactivity than *LRRK2*-p.G2019S in knock-in (KI) mouse embryonic fibroblasts (MEFs, Figure S1). We measured a ~2.5-fold increase in RAB phosphorylation over WT for p.R1441C compared to ~1.5-fold for p.G2019S, representing ~66% greater hyperactivity of the p.R1441C mutation. As expected, the hyperactive kinase activity induced by either the p.R1441C or p.G2019S mutation was effectively inhibited by the LRRK2 kinase inhibitor MLI-2 (Figure S1).

Given the higher level of hyperactivity induced by a R1441-hotspot mutant, we hypothesized that these mutations would more potently disrupt the axonal transport of AVs. To test this hypothesis, we used human induced pluripotent stem cells (iPSCs) from the KOLF2.1J parental line that were gene-edited to a heterozygous knock-in (KI) of the *LRRK2*-p.R1441H mutation by the iPSC Neurodegenerative Disease Initiative (iNDI) at the NIH (Ramos et al., 2021). We differentiated these iPSCs into excitatory glutamatergic neurons using tetracycline-inducible expression of NGN2 (Pantazis et al., 2022), and live-imaged EGFP-LC3-labeled AV transport in the mid-axon at DIV21 (Figure 1A; Video S1). NGN2-induced neurons (iNeurons) express LRRK2 (Bieri et al., 2019; Boecker et al., 2021; Fonseca-Ornelas et al., 2022) and have been used to study the effect of *LRRK2*-p.G2019S on axonal AV dynamics (Boecker et al., 2021).

LRRK2-p.R1441H caused striking changes in the dynamics of axonal AV transport. When scoring the motility and directionality of AV movement (classifications defined in Figure S2A), we found a marked increase in the stationary fraction of AVs at the expense of the retrograde fraction (Figure 1B). In contrast, we did not observe significant changes in net AV directionality in p.G2019S KI iNeurons in our previous work (Boecker et al., 2021). To further explore which transport parameters might be disrupted by *LRRK2*-p.R1441H, we quantified non-processive motility and pausing behavior of motile AVs in WT and p.R1441H KI iNeurons. p.R1441H KI neurons exhibited reduced AV processivity, with higher number of directional reversals (Figure 1C) and significantly increased Δ run length, a metric of non-processive motility calculated as the difference between the total and net run length of each vesicle (Figure S2C; Δ run length defined in S2B). We also observed a ~3-fold increase in the number of pauses per vesicle in p.R1441H KI iNeurons (Figure 1D). While this effect was of similar magnitude to that previously observed in p.G2019S KI iNeurons, the average length of each vesicle's individual pauses (hereafter, pause duration)

Figure 1

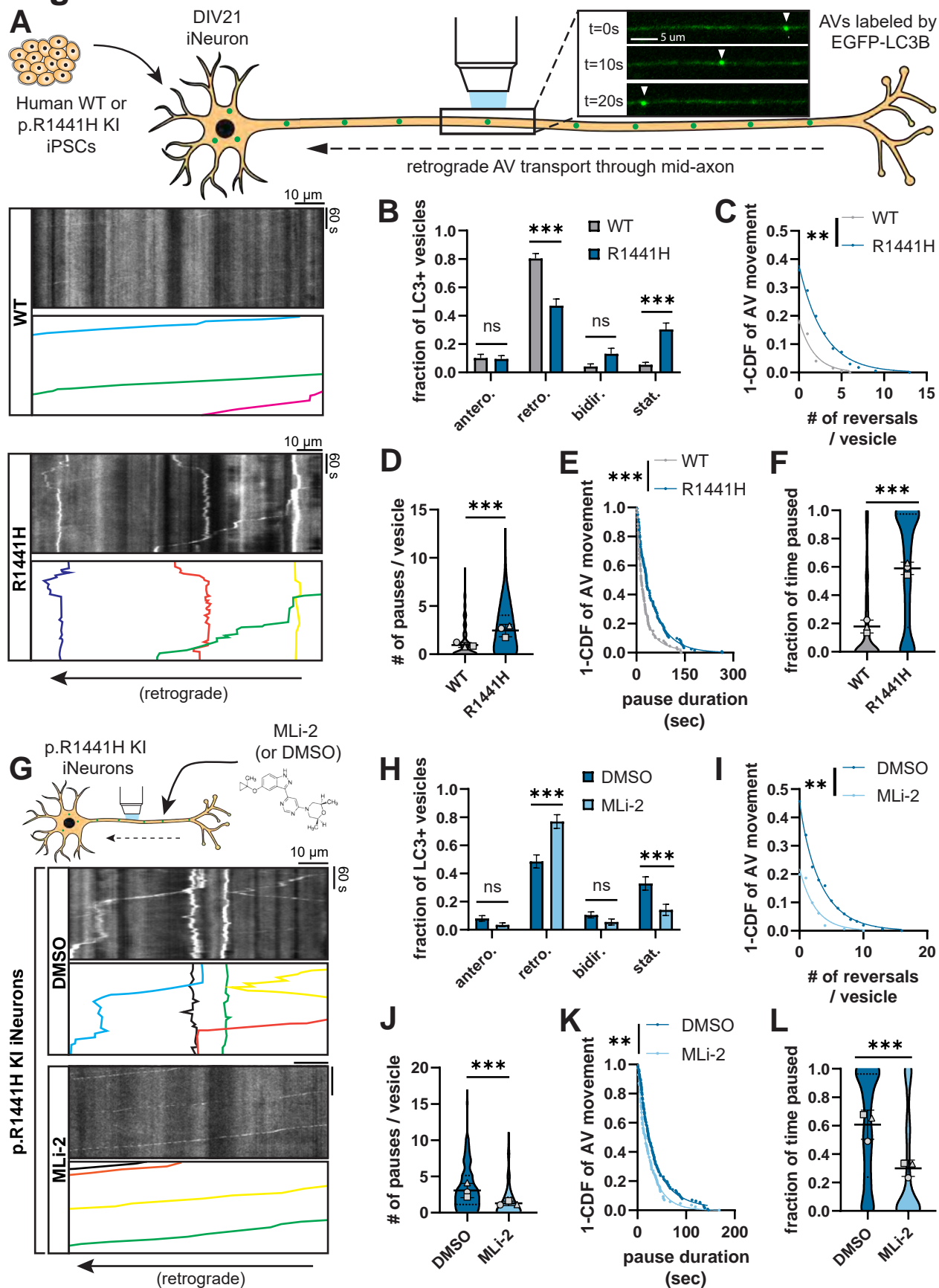


Figure 1. *LRRK2*-p.R1441H knock-in causes kinase-dependent disruption of axonal AV transport.

(A) Top, example time lapse images of EGFP-LC3+ vesicles in the mid-axon of a WT iPSC-derived neuron (iNeuron). Left, kymographs of axonal EGFP-LC3+ vesicles in WT and p.R1441H KI iNeurons. Example AV traces are highlighted. (B) Directionality of AVs in WT and p.R1441H KI iNeurons. Antero., anterograde; retro., retrograde; bidir., bi-directional; stat., stationary (mean \pm SEM; n = 31 neurons from 3 independent experiments; ns, not significant, $p > 0.2026$; *** $p < 0.001$; two-way ANOVA with Sidak's multiple comparisons test). (C-E) Directional reversals (C), pause number (D), and pause duration (E) of motile AVs in WT and p.R1441H KI iNeurons (mean \pm SD for panel D; n = 168-200 motile AVs from 31 neurons from 3 independent experiments; ** $p = 0.00581$; *** $p < 0.001$; mixed effects model analysis, see Methods for specific models used). (F) Fraction of time paused of all AVs in WT and p.R1441H KI iNeurons (mean \pm SD; n = 209-246 AVs from 31 neurons from 3 independent experiments; *** $p < 0.001$; mixed effects model analysis). (G) Kymographs of axonal EGFP-LC3+ vesicles in p.R1441H KI iNeurons treated overnight with DMSO or 100 nM MLI-2. (H) Directionality of AVs in p.R1441H iNeurons treated with DMSO or MLI-2 (mean \pm SEM; n = 30 neurons from 3 independent experiments; ns, not significant, $p > 0.7779$; *** $p < 0.001$; two-way ANOVA with Sidak's multiple comparison test). (I-K) Directional reversals (I), pause number (J), and pause duration (K) of motile AVs in p.R1441H KI iNeurons treated with DMSO or MLI-2 (mean \pm SD for panel J; n = 153-163 motile AVs from 30 neurons from 3 independent experiments; ** $p < 0.00723$; *** $p < 0.001$; mixed effects model analysis). (L) Fraction of time paused of AVs in p.R1441H KI iNeurons treated with DMSO or MLI-2 (mean \pm SD; n = 190-221 AVs from 30 neurons from 3 independent experiments; *** $p < 0.001$; mixed effects model analysis). For panels D, F, J, and L, scatter plot points indicate the means of three independent experiments. For panels C, E, I, and K, curve fits were generated using nonlinear regression (two phase decay).

was increased in p.R1441H KI iNeurons (Figure 1E) but not in p.G2019S KI iNeurons (Boecker et al., 2021).

Thus, expression of the p.R1441H mutation severely disrupted axonal AV transport, with an increased fraction of stationary AVs, an increased number of pauses, and an increase in the pause duration of motile AVs. Combined, these factors manifested as a striking increase in the overall fraction of time that p.R1441H KI AVs spent paused. AVs in p.R1441H KI iNeurons paused for nearly 60% of the time, representing a 3.2-fold increase over WT (Figure 1F). The same quantification performed for AV transport in p.G2019S KI iNeurons (Boecker et al., 2021; data not shown) showed AVs paused for ~40% of the time (1.97-fold over WT). When normalized to corresponding isogenic WT iNeurons, the p.R1441H effect exceeded that of p.G2019S by ~61%, appearing to closely correlate with the ~66% difference in kinase hyperactivity we observed between p.G2019S and a p.R1441 hotspot mutation.

To confirm whether the observed AV transport deficits are LRRK2 kinase activity-dependent, we next tested whether the selective LRRK2 inhibitor MLI-2 (Fell et al., 2015) rescues AV transport in p.R1441H KI iNeurons (Figure 1G). Overnight treatment of iNeurons with 100 nM MLI-2 significantly increased the retrograde fraction of AVs at the expense of the stationary fraction (Figure 1H). Non-processive motility in p.R1441H KI neurons was also rescued, as measured by a reduction of the number of directional reversals and Δ run length (Figure 1I, S2D). Pharmacological LRRK2 inhibition with MLI-2 also reduced pause number and pause duration of motile AVs (Figure 1J-K), rescuing the overall fraction of time spent paused for axonal AVs in p.R1441H KI neurons (Figure 1L). Together, these results are consistent with our previously proposed model of a pathogenic “tug-of-war” between anterograde and retrograde motor proteins induced by hyperactive LRRK2 (Boecker et al., 2021). Importantly, our data also suggest that disruption of AV transport scales in a kinase activity-dependent manner, with greater severity of AV transport defects observed upon expression of p.R1441H as compared to p.G2019S.

Overexpression of the LRRK2-counteracting phosphatase PPM1H rescues axonal AV transport in p.G2019S KI neurons.

Recent work has identified Protein Phosphatase 1H (PPM1H) as the phosphatase counteracting LRRK2 activity through specific dephosphorylation of RAB GTPases (Berndsen et al., 2019). In HEK293 cells transiently expressing LRRK2-p.R1441G, overexpression of GFP-PPM1H^{WT} resulted in reduced levels of phosphothreonine-73 (pT73) RAB10 as compared to overexpression of the catalytically-inactive mutant GFP-PPM1H^{H153D} (Figure S3A). Transient expression of GFP-PPM1H^{WT} in p.G2019S KI MEFs had a similar effect, despite a low transfection efficiency (Figure S3B).

We asked whether enhanced RAB dephosphorylation by PPM1H overexpression could reverse AV transport disruption in neurons expressing hyperactive LRRK2. Using primary cortical neurons from *Lrrk2*-

p.G2019S KI mice, we transiently expressed GFP, GFP-PPM1H^{WT}, or GFP-PPM1H^{H153D} and visualized AV transport in the mid-axon with mScarlet-LC3. We observed co-transport of GFP-PPM1H with LC3-positive AVs along the axon (Figure 2A, S3C, Video S2). Notably, PPM1H^{WT} overexpression improved retrograde AV processivity in p.G2019S KI neurons compared to either GFP mock or PPM1H^{H153D} transfection (Figure 2B, Video S3). Overexpression of GFP-PPM1H^{WT} significantly decreased the number of pauses, pause duration, and overall fraction of time paused of AVs in p.G2019S KI neurons (Fig. 2C-E). GFP-PPM1H^{WT} overexpression also reduced non-processive AV motility as quantified by the number of directional reversals and Δ run length (Figure 2F-G). We did not observe an effect on AV directionality from PPM1H overexpression (Figure S3D). Together, these data indicate that RAB hyperphosphorylation plays a causal role in the disruption of AV transport by hyperactive LRRK2.

PPM1H knock-out phenocopies the effect of hyperactive LRRK2 on AV transport.

To confirm the detrimental effect of RAB hyperphosphorylation on axonal AV transport, we next investigated whether PPM1H knock-out (KO) phenocopies the impairment of AV transport by expression of hyperactive LRRK2. Using the KOLF2.1J parental line, we generated PPM1H KO iPSCs through CRISPR/Cas9 gene editing and differentiated them into excitatory glutamatergic iNeurons (Figure S4A). Western blot with a pan-specific antibody for phosphorylated RAB3A, 8A, 10, 35, and 43 showed elevated levels of LRRK2-phosphorylated RAB proteins in PPM1H KO iNeurons (Figure S4B). Similar to expression of the p.R1441H mutation in LRRK2, PPM1H KO dramatically affected AV directionality, with an increase of the stationary fraction at the expense of the retrograde fraction (Figure 3A-B, Video S4). Furthermore, motile AVs in PPM1H KO iNeurons showed a significant increase in the number of pauses as well as a trend toward increased pause duration that did not achieve statistical significance (Figure 3C-D). Together, increased pausing and number of stationary AVs resulted in a marked increase of the overall fraction of time that PPM1H KO AVs spent paused, reaching a similar level as observed in p.R1441H KI iNeurons (Figure 3E). PPM1H KO also phenocopied the effect of hyperactive LRRK2 on non-processive AV motility, increasing the number of directional reversals and Δ run length of motile AVs (Figure 3F-G).

To verify whether PPM1H KO and LRRK2 hyperactivity disrupt AV transport through the same pathway, we applied MLI-2 to PPM1H KO iNeurons to inhibit LRRK2 kinase activity (Figure 3H). Compared to DMSO control treatment, MLI-2 rescued AV directionality, with retrograde motility restored to the previously stationary fraction (Figure 3I). MLI-2 furthermore decreased the number of pauses and pause duration of motile AVs, restoring the overall fraction of time paused to levels similar to WT iNeurons (Figure 3J-K, S4C). Non-processive motility of motile AVs, as measured by number of directional reversals and Δ run length was also rescued by LRRK2 inhibition (Figure 3L, S4D). In sum, these results from

Figure 2

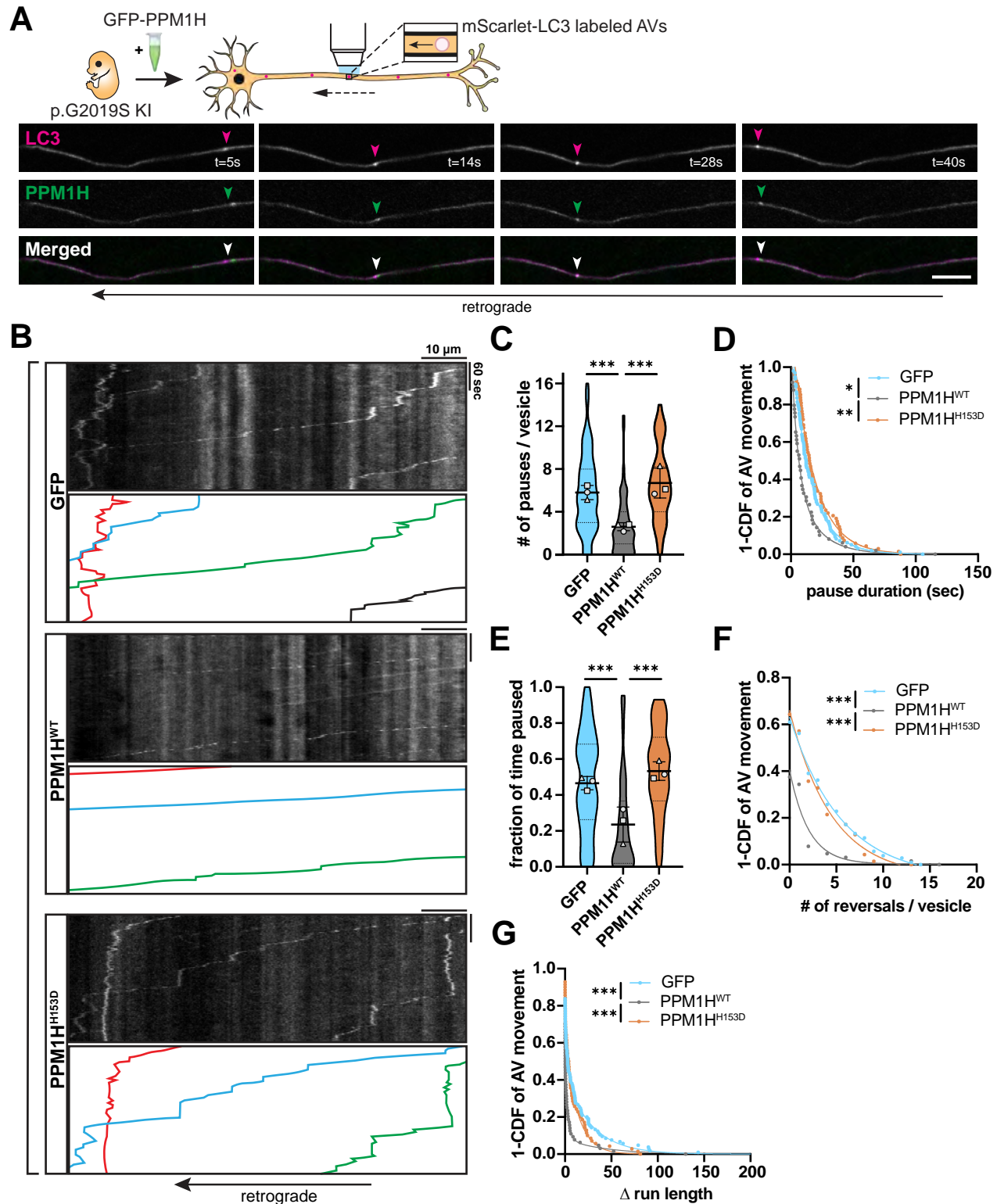


Figure 2. Overexpression of PPM1H rescues AV transport in *Lrrk2*-p.G2019S knock-in mouse cortical neurons. (A) Time lapse images of axonal mScarlet-LC3+ and GFP-PPM1H^{WT}+ vesicles in a p.G2019S KI mouse cortical neuron. Scale bar, 10 μ m. (B) Kymographs of axonal mScarlet-LC3+ vesicles in p.G2019S KI mouse cortical neurons co-expressing GFP, GFP-PPM1H^{WT}, or GFP-PPM1H^{H153D}. Example AV traces are highlighted. (C-G) Pause number (C) and pause duration (D) of motile AVs, fraction of time paused (E) of all AVs, directional reversals (F) and Δ run length (G) of motile AVs in G2019S KI mouse cortical neurons transiently expressing GFP, GFP-PPM1H^{WT}, or GFP-PPM1H^{H153D} (mean \pm SD for panel C and E; n = 66-107 motile AVs (C, D, F, G) and 68-111 total AVs (E) from 21-24 axons from 3 independent experiments; *p=0.01106; **p=0.00144; ***p<0.001; mixed effects model analysis). For panels C and E, scatter plots indicate the means of three independent experiments. For panels D, F, and G curve fits were generated using nonlinear regression (two phase decay for D and F, three phase decay for G).

Figure 3

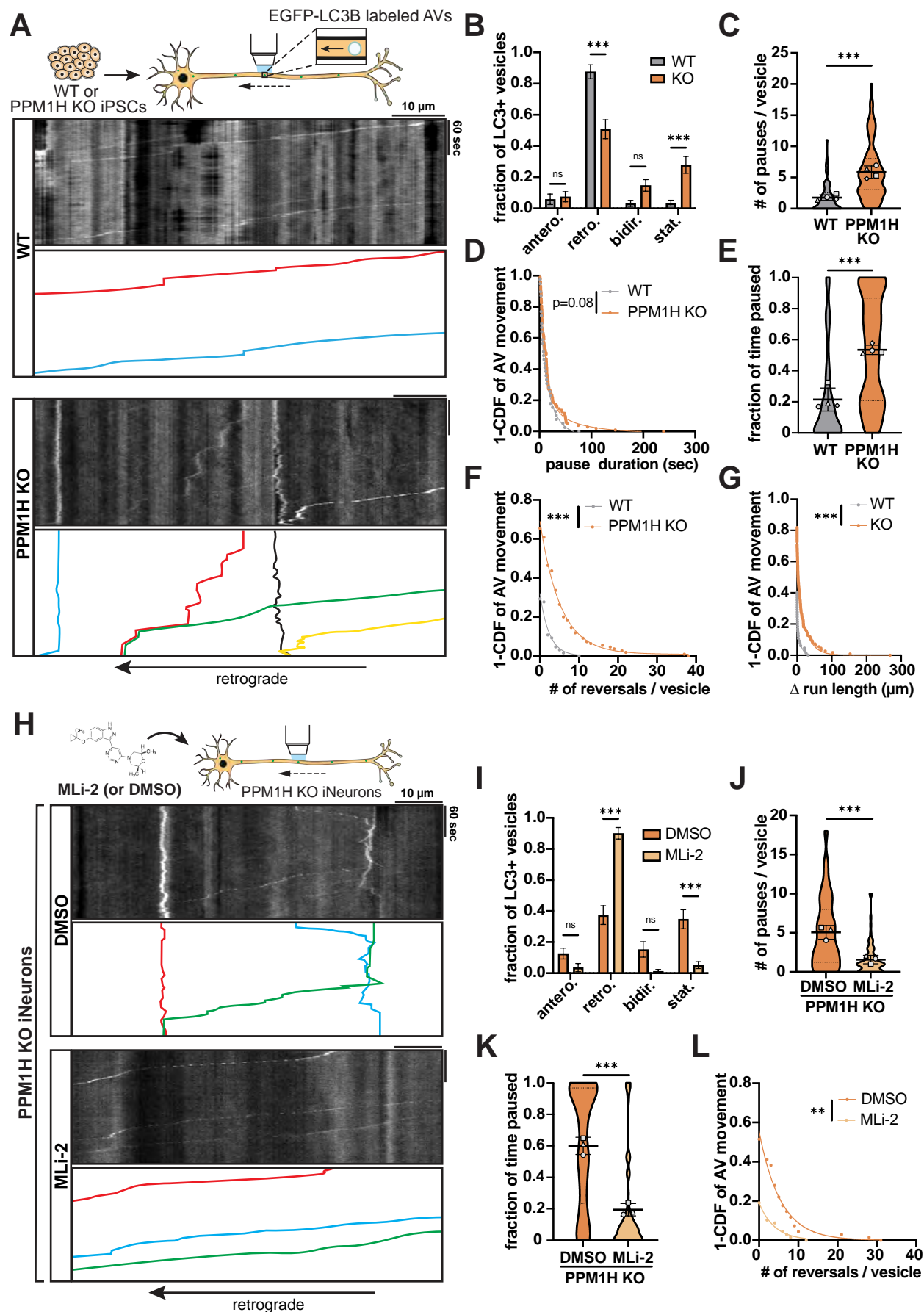


Figure 3. Knock-out of PPM1H causes LRRK2 kinase-dependent disruption of axonal AV transport.

(A) Kymographs of axonal EGFP-LC3+ vesicles in WT and PPM1H KO iNeurons. Example AV traces are highlighted. (B) Directionality of AVs in WT and PPM1H KO iNeurons. Antero., anterograde; retro., retrograde; bidir., bi-directional; stat., stationary (mean \pm SEM; n = 32-39 neurons from 4 independent experiments; ns, not significant, $p > 0.1996$; *** $p < 0.001$; two-way ANOVA with Sidak's multiple comparisons test). (C-G) Pause number (C) and pause duration (D) of motile AVs, fraction of time paused (E) of all AVs, and directional reversals (F) and Δ run length (G) of motile AVs in WT and PPM1H KO iNeurons (mean \pm SD for panel C and E; n = 65-110 motile AVs (C, D, F, G) and 69-141 total AVs (E) from 32-39 neurons from 4 independent experiments; *** $p < 0.001$; mixed effects model analysis). (H) Kymographs of axonal EGFP-LC3+ vesicles in PPM1H KO iNeurons treated over 72 hours with DMSO or 200 nM MLI-2. Example AV traces are highlighted. (I) Directionality of AVs in PPM1H KO iNeurons treated with DMSO or MLI-2 (mean \pm SEM; n = 28-30 neurons from 3 independent experiments; ns, not significant, $p > 0.0772$; *** $p < 0.001$; two-way ANOVA with Sidak's multiple comparison test). (J-L) Pause number (J) of motile AVs, fraction of time paused (K) of all AVs, and directional reversals (L) of motile AVs in PPM1H KO iNeurons treated with DMSO or MLI-2 (mean \pm SD for panel J and K; n = 68 motile AVs (J, L) and 73-104 total AVs (K) from 28-30 neurons from 3 independent experiments; ** $p = 0.00118$; *** $p < 0.001$; mixed effects model analysis). For panel C, E, J, and K, scatter plot points indicate the means of three independent experiments. For panels D, F, G, and L, curve fits were generated using nonlinear regression (two phase decay).

orthogonal PPM1H model systems provide further evidence that RAB GTPase hyperphosphorylation induces disruption of processive retrograde AV transport.

Hyperactive LRRK2 does not disrupt axonal transport of mitochondria.

If pathogenic LRRK2 mutations disrupt axonal transport via hyperphosphorylation of RAB proteins, we would predict that the effect would be cargo-specific, such that cargoes whose transport is not regulated by RABs would not be similarly affected. To this end, we tested whether hyperactive LRRK2 affects the axonal transport of mitochondria, a cargo that undergoes both anterograde and retrograde active transport driven by cytoplasmic dynein and kinesin-1 motors but with no known role for RAB GTPases in regulation of their motility (Fenton et al., 2021). Mitochondrial transport in the axon is also of specific interest given the established role of mitochondrial dysfunction in PD pathophysiology (Bose and Beal, 2016).

We visualized mitochondrial transport in the mid-axon of DIV21 p.R1441H KI iNeurons and isogenic WT neurons with Mito-mEmerald (Figure 4A, Video S5). Similar to our previous characterization of DIV21 iNeurons from a different parental iPSC line (Boecker et al., 2020), ~75% of mitochondria in the mid-axon were stationary or bi-directional in both WT and p.R1441H KI iNeurons. Expression of the p.R1441H mutation neither altered the fraction of motile mitochondria nor perturbed directionality (Figure 4B). We observed a statistically significant but small decrease in axonal mitochondrial density in p.R1441H KI neurons while there was no change in average mitochondrial length (Figure 4C-D), suggesting that the fission/fusion balance of the mitochondrial network was mostly unchanged.

To investigate whether LRRK2-p.R1441H disrupts transport of the motile (anterograde, retrograde, and bi-directional) axonal population of mitochondria, we excluded stationary mitochondria from further analysis. We observed no differences in pause number, pause duration, or Δ run length between WT and p.R1441H KI neurons (Figures 4E-G). Furthermore, there were no direction-specific effects on either the anterograde or retrograde population (Figure S5A-D).

We performed similar live imaging of mitochondrial transport in DIV21 *LRRK2*-p.G2019S KI iNeurons and isogenic WT neurons (Figure S6A). In p.G2019S KI neurons, we observed a small but statistically significant decrease in the stationary fraction of mitochondria, but no change in the anterograde, retrograde, or bi-directional fractions (Figure S6B). Axonal mitochondrial density in p.G2019S KI neurons was slightly higher than in WT neurons (Figure S6C), contrasting with the small decrease in mitochondrial density in p.R1441H KI neurons (Figure 4C) and thus suggesting that these changes are unlikely to be a biologically-significant effect of LRRK2 hyperactivity. There was no change in average mitochondrial length (Figure S6D). Similar to our observations with p.R1441H KI neurons, no changes in pause number, pause duration, or Δ run length of the motile population of axonal mitochondria were observed in p.G2019S

Figure 4

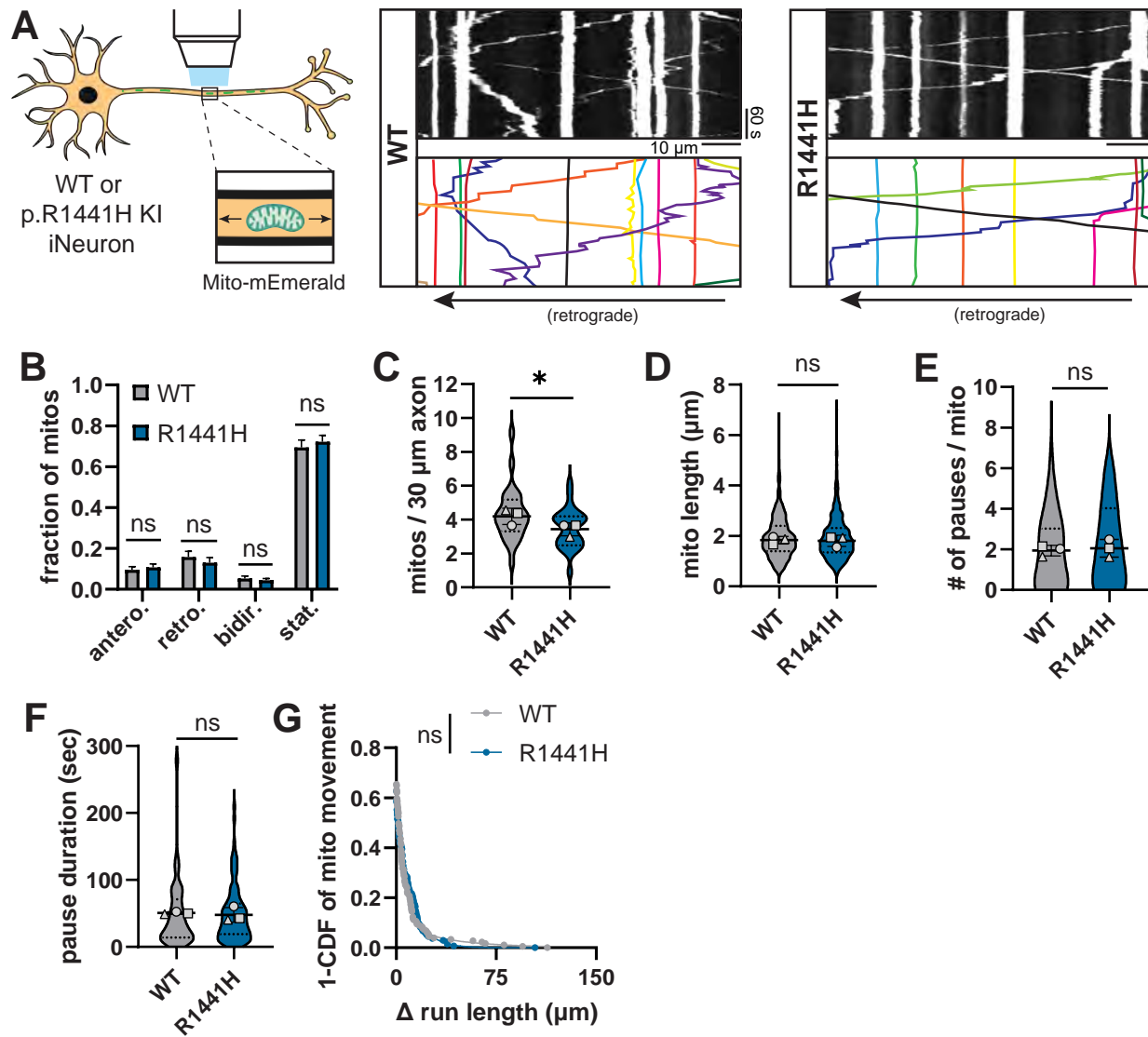


Figure 4. *LRRK2*-p.R1441H does not disrupt axonal mitochondria transport in human iNeurons. (A)

Kymographs of axonal mitochondria labeled by Mito-mEmerald in WT and p.R1441H KI iNeurons. Example mitochondrial traces are highlighted. (B) Directionality of mitochondria in WT and p.R1441H KI iNeurons. Antero., anterograde; retro., retrograde; bidir., bi-directional; stat., stationary (mean \pm SEM; n = 26 neurons from 3 independent experiments; ns, not significant, $p > 0.8700$; two-way ANOVA with Sidak's multiple comparisons test). (C-D) Density per 30 μ m axon (C) and average length (D) of total population of mitochondria in WT and p.R1441H KI iNeurons (mean \pm SD; n = 483-571 mitochondria from 26 neurons from 3 independent experiments; ns, not significant, $p = 0.2918$; * $p = 0.0348$; mixed effects model analysis). (E-G) Pause number (E), pause duration (F), and Δ run length (G) of mitochondria in WT and p.R1441H KI iNeurons (mean \pm SD for panels E-F; n = 136-181 motile mitochondria from 26 neurons from 3 independent experiments; ns, not significant, $p > 0.492$; mixed effects model analysis). For panels C-F, scatter plot points indicate the means of three independent experiments. For panel G, a curve fit was generated using nonlinear regression (two phase decay).

KI neurons (Figure S6E-G). Likewise, p.G2019S KI neurons did not display direction-specific effects on either the anterograde or retrograde population (Figure S5E-H).

In addition to human iNeurons, we also investigated the effect of hyperactive LRRK2 on mitochondrial transport in primary cortical neurons from *Lrrk2*-p.G2019S KI mice. We used Mito-SNAP to visualize mitochondrial transport in the mid-axon of WT and p.G2019S KI mouse cortical neurons treated with DMSO or 100 nM MLI-2 overnight (Figure S6H). We observed no changes in axonal density, average length, or directionality of mitochondria from either p.G2019S KI or MLI-2 application (Figure S6I-K).

In summary, we found that neither the ROC domain mutation *LRRK2*-p.R1441H nor the kinase domain mutation *LRRK2*-p.G2019S affects axonal mitochondrial transport under basal conditions. Together with our previous observations that *LRRK2*-p.G2019S KI does not impair transport of LAMP1-positive vesicles (Boecker et al., 2021), these results underscore the finding that LRRK2 hyperactivity does not indiscriminately disrupt axonal transport, but rather has a cargo-selective effect on autophagic vesicles.

Overexpression of the small GTPase ARF6 ameliorates pRAB-mediated disruption of AV transport.

Processive retrograde AV transport depends on the tight regulation of the opposing activities of two microtubule-associated motor proteins stably bound to autophagosomes. Both the anterograde motor kinesin-1 and the retrograde motor cytoplasmic dynein (in complex with dynactin) are bound to AVs, but adaptor proteins inhibit kinesin and promote dynein activity in WT neurons (Cason et al., 2021; Cheng et al., 2015; Fu et al., 2014; Maday et al., 2012). In our previous work, we found that hyperactive LRRK2 recruits the motor adaptor JIP4, which specifically binds to LRRK2-phosphorylated RAB proteins, to the AV membrane (Boecker et al., 2021; Bonet-Ponce et al., 2020; Kluss et al., 2022; Waschbüsch et al., 2020). This results in abnormal recruitment and activation of kinesin that disrupts processive retrograde AV transport (Boecker et al., 2021).

The active, GTP-bound form of the small GTPase ARF6 binds to the leucine zipper II domain of JIP4 or its closely related paralog JIP3, promoting interaction of JIP3/4 with dynactin while inhibiting the JIP-kinesin interaction (Montagnac et al., 2009). Our group recently found that overexpression of GTP-locked ARF6^{Q67L} did not affect axonal AV transport in WT rat hippocampal neurons, but expression of GDP-locked ARF6^{T27N} decreased retrograde motility of axonal AVs, supporting that there is a role for ARF6 in the regulation of AV transport (Cason and Holzbaur, manuscript in preparation; available upon request). Notably, while JIP3/4 levels were increased on AVs isolated from mice expressing hyperactive LRRK2, ARF6 levels were not (Boecker et al., 2021). We hypothesized that ARF6 levels become limiting in the presence of hyperphosphorylated RABs, and that overexpression of GTP-ARF6 may restore retrograde AV

motility by counterbalancing the abnormally-increased levels of JIP3/4 on the AV membrane (depicted in cartoon in Figure 5A).

To test this model, we transiently expressed the GTP-locked mutant ARF6^{Q67L}-CFP in DIV21 LRRK2-p.R1441H KI iNeurons (Figure 5A, Video S6), and visualized AV transport in the mid-axon with EGFP-LC3B. In the CFP mock condition, we again observed dramatic disruption of retrograde AV transport associated with p.R1441H KI. However, overexpression of ARF6^{Q67L} significantly ameliorated this disruption, increasing the retrograde fraction of AVs at the expense of the stationary fraction (Figure 5B). ARF6^{Q67L} expression also reduced pausing behavior of motile AVs, reflected by decreases in number of pauses and pause duration (Figure 5C-D). Reduced pausing and stationary fraction resulted in an overall decrease in the fraction of time p.R1441H KI AVs spent paused (Figure 5E). Non-processive motility was also decreased by ARF6^{Q67L} expression, as quantified by directional reversals and Δ run length (Figure 5F-G). For each metric of AV transport, ARF6^{Q67L}-expressing iNeurons approached but did not reach WT levels (Figure 1), consistent with a partial rescue of the phenotype in p.R1441H KI neurons.

Next, we transiently expressed ARF6^{Q67L}-CFP or CFP-only in DIV21 PPM1H KO iNeurons (Figure 6A). Similar to overexpression of ARF6 in p.R1441H KI iNeurons, the retrograde fraction was increased, and the stationary fraction was decreased (Figure 6B). Likewise, we observed significant decreases in number of pauses, overall fraction of time paused, number of directional reversals, and Δ run length. We did not observe a change in the pause duration in PPM1H KO iNeurons as a result of ARF6^{Q67L} expression (Figure 6C-G). Thus, in two different models of elevated LRRK2-mediated RAB phosphorylation, overexpression of ARF6 partially rescued retrograde axonal transport of AVs. Overall, our findings support a model where increased levels of phosphorylated RABs cause recruitment of additional JIP3/4, which recruits and activates kinesin in the absence of ARF6 regulation. This induces an inappropriately-regulated “tug-of-war” that disrupts processive retrograde AV transport. Overexpression of GTP-ARF6 switches surplus JIP3/4 to an activator of dynein/dynactin instead of kinesin and thereby restores AV processivity.

Figure 5

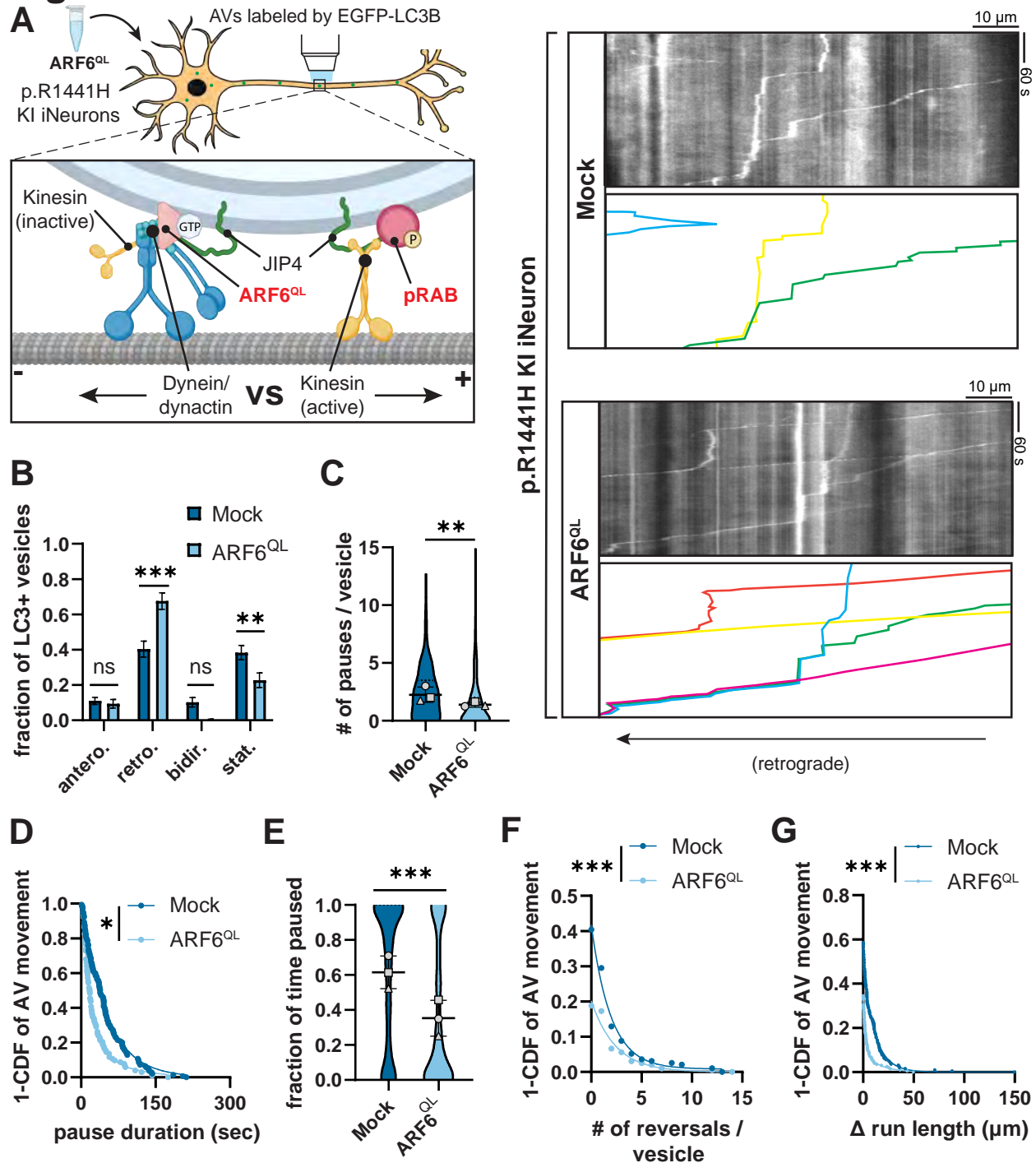


Figure 5. Overexpression of ARF6^{Q67L} ameliorates AV transport deficits in *LRRK2*-p.R1441H KI iNeurons. (A) Kymographs of axonal EGFP-LC3⁺ vesicles in p.R1441H KI iNeurons transiently expressing CFP (“Mock”) or ARF6^{Q67L}-CFP. Example AV traces are highlighted. Cartoon depicts competition between ARF6^{Q67L} and phospho-RAB for binding with JIP4, with opposing directionality of binding partner motors. (B) Directionality of AVs in p.R1441H KI iNeurons transiently expressing CFP or ARF6^{Q67L}-CFP. Antero., anterograde; retro., retrograde; bidir., bi-directional; stat., stationary (mean \pm SEM; n = 27-28 neurons from 3 independent experiments; ns, not significant, $p > 0.1492$; ** $p = 0.0053$; *** $p < 0.0001$; two-way ANOVA with Sidak’s multiple comparisons test). (C-D) Pause number (C) and pause duration (D) of motile AVs in p.R1441H KI iNeurons transiently expressing CFP or ARF6^{Q67L}-CFP (mean \pm SD for panel C; n = 195-199 motile AVs from 27-28 neurons from 3 independent experiments; * $p = 0.0123$; ** $p = 0.00261$; mixed effects model analysis). (E) Fraction of time paused of all AVs in p.R1441H KI iNeurons transiently expressing CFP or ARF6^{Q67L}-CFP (mean \pm SD; n = 257-321 AVs from 27-28 neurons from 3 independent experiments; *** $p < 0.001$; mixed effects model analysis). (F-G) Directional reversals (F) and Δ run length (G) of motile AVs in p.R1441H KI iNeurons transiently expressing CFP or ARF6^{Q67L}-CFP (n = 195-199 motile AVs from 27-28 neurons from 3 independent experiments; *** $p < 0.001$; mixed effects model analysis). For panels C and E, scatter plot points indicate the means of three independent experiments. For panels D, F, and G, curve fits were generated using nonlinear regression (two phase decay).

Figure 6

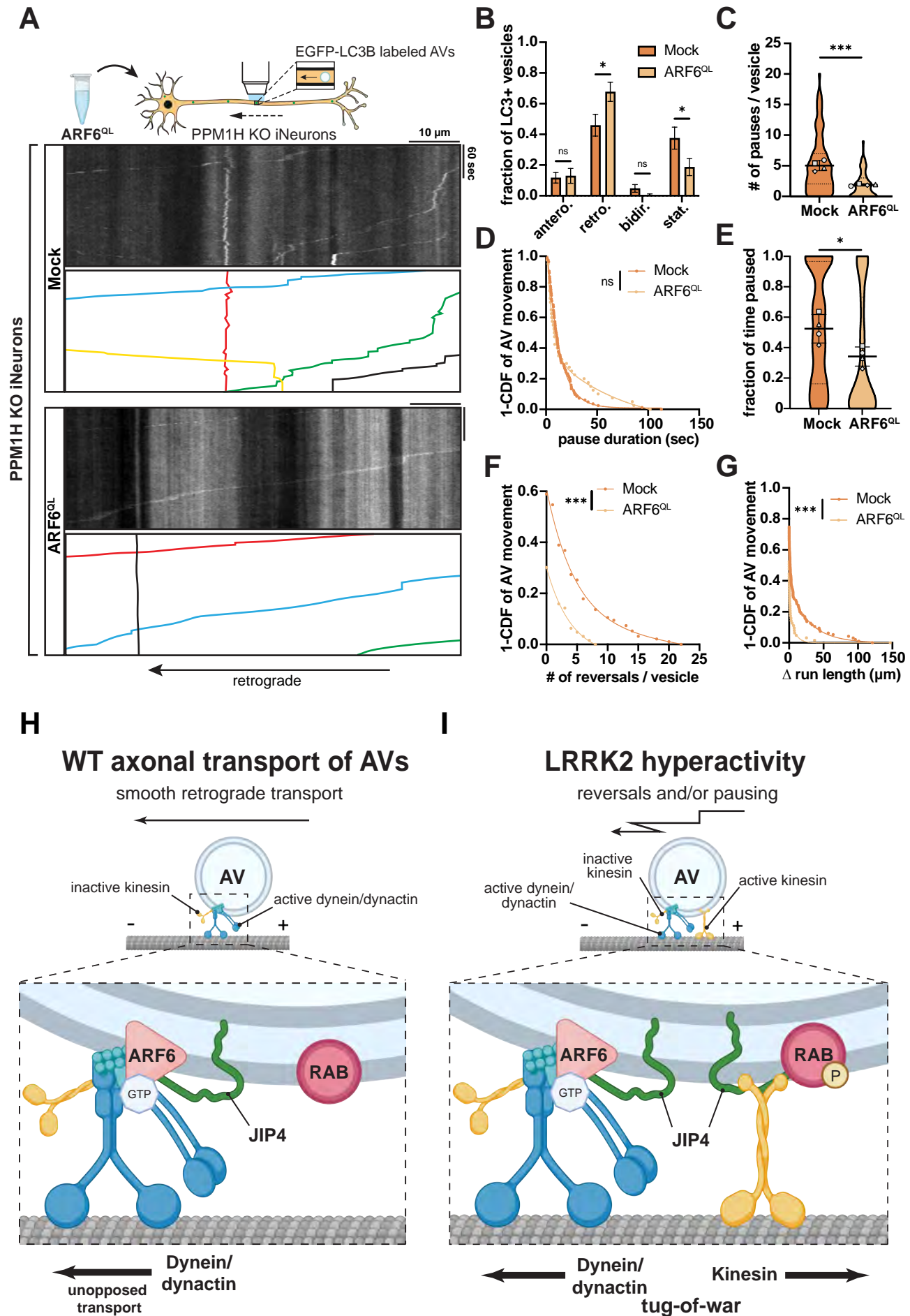


Figure 6. Overexpression of ARF6^{Q67L} ameliorates AV transport deficits in PPM1H KO iNeurons.

(A) Kymographs of axonal EGFP-LC3⁺ vesicles in PPM1H KO iNeurons transiently expressing CFP (“Mock”) or ARF6^{Q67L}-CFP. Example AV traces are highlighted. (B) Directionality of AVs in PPM1H KO iNeurons transiently expressing CFP or ARF6^{Q67L}-CFP. Antero., anterograde; retro., retrograde; bidir., bi-directional; stat., stationary (mean \pm SEM; n = 32-34 neurons from 4 independent experiments; ns, not significant, $p > 0.9652$; * $p < 0.0410$; two-way ANOVA with Sidak’s multiple comparisons test). (C-G) Pause number (C) and pause duration (D) of motile AVs, fraction of time paused (E) of all AVs, and directional reversals (F) and Δ run length (G) of motile AVs in PPM1H KO iNeurons transiently expressing CFP or ARF6^{Q67L}-CFP (mean \pm SD for panel C and E; n = 63-95 motile AVs (C, D, F, G) and 77-134 total AVs (E) from 32-34 neurons from 4 independent experiments; ns, not significant, $p = 0.638$; * $p = 0.0396$; *** $p < 0.001$; mixed effects model analysis). For panels C and E, scatter plot points indicate the means of four independent experiments. For panels D, F, and G, curve fits were generated using nonlinear regression (two phase decay). (H-I) Model: imbalance between ARF6 and pRABs disrupts axonal AV transport in conditions of LRRK2 hyperactivity (H) Under physiologic conditions, ARF6 binds to JIP4, promoting JIP4 binding to dynactin while discouraging the JIP4-kinesin interaction. With active dynein/dynactin and inactive kinesin, AVs undergo smooth retrograde transport in WT neurons. (I) Under pathologic conditions of LRRK2 hyperactivity, increased phosphorylation of RAB GTPases on the AV membrane leads to increased recruitment of JIP4, due to specific binding of JIP4 by RABs in their phosphorylated state. This allows for recruitment and disinhibition of kinesin by JIP4. The presence of active dynein/dynactin and active kinesin on the same organelle results in an unproductive tug-of-war between microtubule-associated motors, leading to non-processive motility and pausing behavior of AVs.

DISCUSSION

A growing body of evidence links pathogenic LRRK2 mutations to hyperphosphorylation of RAB GTPases, but it remains unclear how phospho-RABs contribute to pathogenesis in PD. Here, we show that increased levels of LRRK2-phosphorylated RAB proteins, resulting from an imbalance in LRRK2 kinase and PPM1H phosphatase activity, disrupt the axonal transport of autophagosomes. Our results further implicate a role for ARF6 in regulating retrograde AV transport (Figure 6H), as expression of GTP-locked ARF6 partially rescued transport deficits. We propose that LRRK2-mediated hyperphosphorylation of RAB GTPases induces dysregulation of the opposing motors dynein and kinesin at the AV membrane in a pathogenic “tug-of-war”. Increased recruitment of JIP3/4 in the absence of enhanced levels of ARF6 inappropriately activates kinesin (Figure 6I), which manifests as increased pausing behavior and non-processive motility of axonal AVs.

We found that *LRRK2*-p.R1441H, a kinase-hyperactivating mutation located in the LRRK2 Roc domain, disrupted axonal AV transport to an even greater extent than the p.G2019S mutation we studied in previous work. While both p.G2019S and p.R1441H increased pause frequency and non-processive motility, only p.R1441H increased average duration of individual pauses and fraction of AVs remaining stationary. Our data suggest that there is an exacerbation of the severity of pausing behavior in the presence of the more hyperactive mutant LRRK2, to the point where a greater fraction of AVs appears to be fully stationary during the confines of a 5-minute live-imaging recording. Combined, the overall fraction of time that AVs spent paused in p.R1441H KI neurons exceeded the effect of p.G2019S by more than 60%. Considering that p.R1441 hotspot mutations cause significantly higher levels of kinase hyperactivity than p.G2019S, our data indicate that the magnitude of AV transport deficits may scale with the level of RAB hyperphosphorylation.

LRRK2 hyperactivity selectively affects axonal cargoes, as autophagosome motility is significantly altered by either hyperactivating mutations in LRRK2 or by loss of the countering phosphatase, but no changes were observed in mitochondrial transport or in lysosome trafficking (Boecker et al., 2021). We hypothesize that AV motility is specifically disrupted because it is regulated by one or more of the RABs that are LRRK2 substrates. In contrast, there is no known role for RAB binding in the mechanism of axonal trafficking of healthy mitochondria, which is controlled by a complex containing the outer mitochondrial membrane protein Miro, the motor adaptor TRAK, and the motor proteins kinesin-1 and dynein/dynactin (Fenton et al., 2021). It is important to note that our live-imaging experiments were all performed at basal conditions, in the absence of pharmacologically-induced mitochondrial damage. It has previously been reported that in the presence of high levels of prolonged mitochondrial stress, p.G2019S KI may alter clearance of axonal mitochondria by impairing degradation of Miro and thereby preventing adequate arrest of motile mitochondria (Hsieh et al., 2016). Further investigation is needed to determine whether such an

effect is shared by other pathogenic mutants and whether it can be detected at physiologically-relevant levels of mitochondrial damage.

In PPM1H KO iNeurons, the absence of a key phosphatase opposing LRRK2 activity causes increased levels of pRABs in the setting of LRRK2^{WT} (Figure S4B). In a recent study, loss of PPM1H was found to phenocopy the effects of hyperactive LRRK2 on pRAB-dependent ciliation in mouse cholinergic neurons and astrocytes (Khan et al., 2021). Here, we found that loss of PPM1H caused marked deficits of retrograde AV transport in iNeurons, phenocopying the effect of hyperactive LRRK2 on organelle motility. Defective transport was rescued by treatment with MLI-2, confirming that the alterations in AV transport induced by loss of PPM1H are dependent on LRRK2-mediated RAB phosphorylation. The most likely RABs involved in the LRRK2-dependent impairment of AV transport are RAB10 and/or RAB35, as these RABs are dephosphorylated by PPM1H (Berndsen et al., 2019) and have been implicated in the recruitment of JIP3/4 to organelles (Bonet-Ponce et al., 2020; Waschbüsch et al., 2020). Proteomic and Western blot analyses indicate that RAB10 and RAB35 as well as PPM1H and LRRK2 are all associated with the outer membrane of AVs isolated from brain lysates (Boecker et al., 2021; Goldsmith et al., 2022). However, we cannot exclude the possibility that an as yet unidentified pRab is involved. We note that the AV transport phenotype observed in PPM1H KO neurons more closely resembled the transport deficits seen in p.R1441H KI (this study) rather than the more limited disruption seen previously in p.G2019S KI neurons. This is likely due to the potent increase in levels of pRABs that we and others observed upon PPM1H KO (Khan et al., 2021). Overall, our data imply an important balance between LRRK2 and PPM1H activity in the regulation of AV transport. In both PPM1H KO and p.R1441H KI iNeurons, we found that overexpression of the active, GTP-locked mutant ARF6^{QL} ameliorates defects in AV transport. GTP-ARF6 favors the interaction of JIP3/4 with dynein/dynactin rather than kinesin (Montagnac et al., 2009) and is thus well-positioned as a regulatory switch that promotes uncontested retrograde AV transport. Recent work supports a role for ARF6 in the regulation of AV transport in neurons, as overexpression of the inactive, GDP-locked mutant ARF6^{T27N} impairs retrograde AV transport along the axon (Cason and Holzbaur, manuscript in preparation; available upon request). We propose that hyperphosphorylated RABs disrupt AV transport by recruiting additional JIP3/4 to the AV membrane, leading to erroneous activation of kinesin and causing an unregulated “tug-of-war” between anterograde and retrograde motor proteins, while overexpressed GTP-ARF6 acts as a switch to favor the JIP3/4-dependent activation of dynein/dynactin, thereby restoring highly processive retrograde motility.

How may defects in axonal AV transport be tied to neurodegeneration in PD? The processive transport of AVs is tightly linked to their function as degradative organelles (Cason and Holzbaur, 2022; Cason et al., 2021). Disruption of AV transport induces defective AV acidification and impaired autophagosomal cargo degradation across multiple models of neurodegenerative disease (Boecker et al.,

2021; Fu et al., 2014; Wong and Holzbaur, 2014). Recent proteomic work has identified nucleoid-enriched mitochondrial fragments as a main cargo of basal autophagy in neurons (Goldsmith et al., 2022). Thus, defects in neuronal autophagy may lead to the aberrant accumulation of mitochondrial DNA (mtDNA) with the potential to stimulate pro-inflammatory pathways (Riley and Tait, 2020) and thus contribute to the inflammation characteristic of PD progression (Wallings and Tansey, 2019). The degradation of other cargos may also be affected, including the synaptically-enriched protein alpha-synuclein, a key protein in PD pathology and an established substrate of autophagy (Farfel-Becker et al., 2019; Friedman et al., 2012; Vogiatzi et al., 2008). Consistent with this possibility, exacerbated alpha-synuclein aggregation has been linked to expression of hyperactive LRRK2 (Bieri et al., 2019; Ho et al., 2022; MacIsaac et al., 2020; Schapansky et al., 2018; Volpicelli-Daley et al., 2016). Ongoing work to examine the degradation of alpha-synuclein in cellular and animal models of PD should shed further light on this question.

In summary, our data directly link LRRK2-mediated hyperphosphorylation of RAB GTPases to disruption of retrograde AV transport. Mechanistically, we propose that an imbalance between ARF6 and JIP3/4, recruited to the AV membrane by phospho-RABs, disrupts AV transport by inducing an unproductive “tug-of-war” between anterograde and retrograde motor proteins. Our results indicate that the severity of AV transport deficits may scale with the level of LRRK2 hyperactivity, and our data reveal an important balance between LRRK2 kinase activity and the LRRK2-opposing phosphatase PPM1H in regulating AV transport. Together, our work provides new insights on how multiple potential therapeutic targets interact in a pathological mechanism that disrupts axonal autophagy, a homeostatic pathway essential for neuronal health and function.

ACKNOWLEDGEMENTS

We thank Mariko Tokito for assistance in the cloning of plasmid constructs, Karen Wallace Jahn for assistance with animal models, and Cooper Penner for optimizing our custom KymoTracer analysis software. We thank Michael Ward (National Institutes of Health) and Bill Skarnes (The Jackson Laboratory) for expertise in utilizing resources from the iPSC Neurodegeneration Initiative (iNDI), and the Live-Cell Imaging Facility of the Max Planck Institute for Multidisciplinary Sciences, Goettingen, Germany for technical support. Cartoon schematics were created in part with BioRender.com. Protein structures in graphical abstract were supplied from UniProt.org under the Creative Commons Attribution 4.0 International (CC BY 4.0) License (PDB 7LHT for LRRK2, 7L4J for PPM1H, and 2J5X for ARF6). This work was supported by the National Institutes of Health (1 F31 NS124249-01 and T32-AG-000255 to D.D., R35 GM126950 to E.L.F.H.), the Michael J. Fox Foundation (MJFF-021130 to C.A.B. and E.L.F.H., MJFF-15100 and MJFF-019411 to E.L.F.H.), the German Research Foundation (DFG; BO 5434/2-1 to C.A.B.), and the Howard Hughes Medical Institute (Hanna Gray Fellowship to C.S.E.). The E.L.F.H. laboratory is funded by the joint efforts of The Michael J. Fox Foundation for Parkinson's Research (MJFF) and the Aligning Science Across Parkinson's (ASAP) initiative. MJFF administers the grant ASAP-000350 on behalf of ASAP and itself.

AUTHOR CONTRIBUTIONS

Conceptualization, D.D., C.A.B., and E.L.F.H.; methodology, D.D. and C.A.B.; investigation, D.D., C.A.B., E.M.S., C.S.E.; writing – original draft, D.D., C.A.B., and E.L.F.H.; writing – review and editing, D.D., C.A.B., E.M.S., C.S.E., and E.L.F.H.; funding acquisition, D.D., C.A.B., and E.L.F.H.; supervision, C.A.B. and E.L.F.H.

DECLARATION OF INTERESTS

The authors declare no competing interests.

STAR METHODS

KEY RESOURCES TABLE

REAGENT or RESOURCE	SOURCE	IDENTIFIER
Antibodies		
Anti-RAB10, Rabbit Monoclonal	Abcam	Cat# ab237703, RRID:AB_2884879
Anti-RAB10 (phospho T73), Rabbit Monoclonal	Abcam	Cat# ab230261, RRID:AB_2811274
Anti-RAB8A (phospho T72), Rabbit Monoclonal	Abcam	Cat# ab230260, RRID:AB_2814988
Anti-PPM1H, Sheep Polyclonal	MRC PPU reagents and services, University of Dundee, Scotland	#DA018, 3 rd bleed, RRID:AB_2923281
Anti-Rabbit IgG-IRDye 800CW, Donkey Polyclonal	Li-COR Biosciences	Cat# 926-32213, RRID:AB_621848
Anti-Rabbit IgG-IRDye 680RD, Donkey Polyclonal	Li-COR Biosciences	Cat# 926-68073, RRID:AB_10954442
Anti-Mouse IgG-IRDye 800CW, Donkey Polyclonal	Li-COR Biosciences	Cat# 926-32212, RRID:AB_621847
Anti-Sheep Alexa Fluor 680, Donkey Polyclonal	Thermo Fisher	Cat# A21102, RRID:AB_10374469
Chemicals, Peptides, and Recombinant Proteins		
MLi-2	Tocris	Cat# 5756
DMSO	Sigma-Aldrich	Cat# D2650
PLL (mol wt 70,000 – 150,000)	Sigma-Aldrich	Cat# P1274
HBSS (10x)	Thermo Fisher	Cat# 14185-052
1M HEPES	Thermo Fisher	Cat# 15630-080
2.5% Trypsin	Thermo Fisher	Cat# 15090-046
Minimum essential medium (MEM)	Thermo Fisher	Cat# 11095-072
Horse serum (heat inactivated)	Thermo Fisher	Cat# 16050-122
Sodium pyruvate	Corning	Cat# 36017004
D-Glucose solution 45%	Sigma-Aldrich	Cat# G8769
GlutaMAX	Thermo Fisher	Cat# 35050061
B27 Supplement	Thermo Fisher	Cat# 17504-044
Neurobasal Medium	Thermo Fisher	Cat# 21103-049
Penicillin-Streptomycin	Thermo Fisher	Cat# 15140-122
AraC	Sigma-Aldrich	Cat# C6645
Lipofectamine 2000 Transfection Reagent	Thermo Fisher	Cat# 11668019
Matrigel Growth Factor Reduced	Corning	Cat# 354230
Essential 8 Medium	Thermo Fisher	Cat# A1517001
mTeSR Medium	Stemcell Technologies	Cat# 85850
Alt-R HiFi Cas9 Nuclease V3	IDT	Cat# 1081060
ReLeSR	Stemcell Technologies	Cat# 05872
Accutase	Sigma-Aldrich	Cat# A6964
ROCK Inhibitor Y-27632	Selleckchem	Cat# S1049
Tet System Approved FBS	Takara	Cat# 631107
Knockout Serum Replacement	Thermo Fisher	Cat# 10828010
DMEM/F-12, HEPES	Thermo Fisher	Cat# 11330032
N2 Supplement	Thermo Fisher	Cat# 17502048
Non-essential Amino Acids (NEAA)	Thermo Fisher	Cat# 11140050

Doxycycline	Sigma-Aldrich	Cat# D9891
Poly-L-Ornithine	Sigma-Aldrich	Cat# P3655
BrainPhys Neuronal Medium	Stemcell Technologies	Cat# 05790
Laminin	Corning	Cat# 354232
BDNF	PeptoTech	Cat# 450-02
NT-3	PeptoTech	Cat# 450-03
Lipofectamine Stem Transfection Reagent	Thermo Fisher	Cat# STEM00003
Microcystin-LR	Sigma-Aldrich	475815
Halt Protease and Phosphatase Inhibitor Cocktail	Thermo Fisher	78442
5-Fluoro-2'-deoxyuridine	Sigma-Aldrich	F0503
Uridine	Sigma-Aldrich	U3003
Critical Commercial Assays		
BCA Protein Assay Kit	Thermo Fisher	Cat# 23225
Plasmid Maxi Kit	QIAGEN	Cat# 12163
Experimental Models: Cell Lines		
Human: NGN2 iPSCs	M. Ward (National Institutes of Health)(Wang et al., 2017)	N/A
Human: LRRK2-G2019S NGN2 iPSCs (heterozygous)	(Boecker et al., 2021)	N/A
Human: LRRK2-WT NGN2 iPSCs	(Boecker et al., 2021)	N/A
Mouse: LRRK2-G2019S knock-in MEFs	(Boecker et al., 2021)	N/A
Mouse: WT MEFs	MRC PPU reagents and services, University of Dundee, Scotland	N/A
Mouse: LRRK2-R1441C knock-in MEFs	MRC PPU reagents and services, University of Dundee, Scotland	N/A
Human: KOLF2.1J WT iPSCs	B. Skarnes (Jackson Laboratories, Connecticut)	N/A
Human: KOLF2.1J LRRK2-R1441H iPSCs	B. Skarnes (Jackson Laboratories, Connecticut)	N/A
Human: KOLF2.1J PPM1H KO iPSCs	This paper	N/A
Experimental Models: Organisms/Strains		
Mouse: LRRK2-G2019S knock-in	Taconic	Model #13940
Mouse: C57BL/6NTac WT	Taconic	Model #B6
Oligonucleotides		
Gene knockout kit v2 – PPM1H (human)	Synthego	N/A
Recombinant DNA		
Plasmid: PGK EGFP-LC3B	Modified from PGK mCherry-LC3B (gift from Michael Ward, NIH)	Addgene plasmid #193025
Plasmid: PGK ARF6 ^{Q67L} -CFP	This paper	Addgene plasmid #193026 (modified from Addgene plasmid #11387)

Plasmid: PGK CFP	This paper	Addgene plasmid #193027 (modified from Addgene plasmid #11387)
Plasmid: PGK 4xMito-mEmerald	This paper	Addgene plasmid #193028 (modified from Addgene plasmid #98818)
Plasmid: CMV mScarlet-LC3B	Modified from EGFP-LC3B (gift from T. Yoshimori, Osaka University, Japan)	Addgene plasmid #193029
Plasmid: CMV EGFP-PPM1H-WT	MRC PPU reagents and services, University of Dundee, Scotland	#DU62939
Plasmid: CMV EGFP-PPM1H-H153D	This paper	Addgene plasmid #193030 (modified from MRC PPU #DU66215)
Plasmid: CMV FLAG-LRRK2-R1441G	MRC PPU reagents and services, University of Dundee, Scotland	#DU13077
Plasmid: PB-TO-hNGN2	Gift from iPSC Neurodegenerative Disease Initiative (iNDI) & Michael Ward	Addgene plasmid #172115
Plasmid: piggyBac™ transposase vector	Transposagen	N/A
Software and Algorithms		
FIJI (Release 2.9.0)	NIH, USA	https://imagej.net/Fiji
Prism 9	GraphPad	https://www.graphpad.com/scientific-software/prism/
RStudio: Integrated Development for R (2021.09.2 Build 382)	RStudio Team	http://www.rstudio.com/
Matlab R2022a	MathWorks	https://www.mathworks.com/products/matlab.html
KymoSuite (custom Matlab script)	(Guedes-Dias et al., 2019)	https://github.com/jnirschl/kinesin-3_guedes-dias_2018
Volocity	PerkinElmer	https://www.perkinelmer.com
VisiView 5.0.0.24	Visitron	https://www.visitron.de/products/visiviewr-software.html
Adobe Illustrator 2022	Adobe	https://www.adobe.com/products/illustrator.html
BioRender	BioRender	https://biorender.com/
Other		
35 mm #1.5 glass bottom imaging dishes	MatTek	Cat# P35G-1.5-20-C

RESOURCE AVAILABILITY

Lead Contact

Further information and requests for resources and reagents should be directed to and will be fulfilled by the lead contacts, C. Alexander Boecker (alexander.boecker@med.uni-goettingen.de) and Erika L. F. Holzbaur (holzbaur@pennmedicine.edu).

Materials Availability

Unique reagents generated in this study are available from the Lead Contacts with a completed Materials Transfer Agreement.

Data and Code Availability

Primary data that is presented in this study has been deposited in Zenodo and repository and can be accessed using the Digital Object Identifier 10.5281/zenodo.7178198. The custom MATLAB scripts used in this study to manually track kymographs (KymoSuite) are available at https://github.com/jnirschl/kinesin-3_guedes-dias_2018/tree/master/kymoSuite. Protocols have been deposited to Protocols.io (link will be generated and placed here after formatting of these protocols by Protocols.io staff).

EXPERIMENTAL MODEL AND SUBJECT DETAILS

Primary neuron culture

All experiments were performed following protocols approved by the Institutional Animal Care and Use Committee at the University of Pennsylvania. *Lrrk2*-p.G2019S KI mice (model #13940) and B6NTac mice (model #B6) were obtained from Taconic, Cambridge City, Indiana production site. Mouse cortices were dissected from homozygous WT or *Lrrk2*-p.G2019S embryos of either sex at day 15.5. Cortical neurons were isolated by digestion with 0.25% Trypsin and trituration through a small-bore serological pipette. Neurons were plated on 35 mm glass-bottom imaging dishes (P35G-1.5-20-C; MatTek) in Attachment Media (MEM supplemented with 10% horse serum, 33 mM D-glucose and 1 mM sodium pyruvate). After 5 hours, Attachment Media was replaced with Maintenance Media (Neurobasal [GIBCO] supplemented with 2% B-27 [GIBCO], 33 mM D-glucose [Sigma], 2 mM GlutaMAX [GIBCO], 100 U/mL penicillin and 100 mg/mL streptomycin [Sigma]). AraC (1 μ M) was added the day after plating to prevent glia cell proliferation. 40% of the media was replaced with fresh Maintenance Media twice per week. Transfections of DIV6 mouse cortical neurons were performed 16-24 hours before imaging using Lipofectamine 2000 Transfection Reagent (ThermoFisher) and 0.9 μ g total plasmid DNA.

i³Neuron differentiation

Pre-i³Neuron iPSCs (human iPSCs with an integrated doxycycline-inducible mNGN2 transgene in the AAVS1 safe-harbor locus) were a gift from M. Ward (National Institutes of Health, Maryland) and have

been described previously (Boecker et al., 2020, 2021; Fernandopulle et al., 2018). Cytogenetic analysis of G-banded metaphases cells showed a normal male karyotype (Cell Line Genetics). Mycoplasma testing was negative. Pre-i³N iPSCs were cultured on plates coated with Growth Factor Reduced Matrigel (Corning) and fed daily with Essential 8 media (ThermoFisher). Differentiation of iPSCs into i³Neurons was performed using an established protocol (Fernandopulle et al., 2018). In brief, iPSCs were passaged using Accutase (Sigma) and plated on Matrigel-coated dishes in Induction Media (DMEM/F12 supplemented with 1% N2-supplement [GIBCO], 1% NEAA [GIBCO], and 1% GlutaMAX [GIBCO], and containing 2 µg/mL doxycycline. After 72 hours of doxycycline exposure, i³Neurons were dissociated with Accutase and cryo-preserved in liquid N₂.

Piggybac-mediated iPSC-derived neuron differentiation

KOLF2.1J-background WT and *LRRK2*-p.R1441H KI iPSCs were a gift from B. Skarnes (Jackson Laboratories, Connecticut) as part of the iPSC Neurodegenerative Disease Initiative (iNDI) and have been described previously (Pantazis et al., 2022). KOLF2.1J-background PPM1H KO iPSCs were generated as described below. Cytogenetic analysis of G-banded metaphases cells showed a normal male karyotype (Cell Line Genetics). Mycoplasma testing was negative. iPSCs were cultured on plates coated with Growth Factor Reduced Matrigel (Corning) and fed daily with Essential 8 media (ThermoFisher). To stably express doxycycline-inducible hNGN2 using a PiggyBac delivery system, iPSCs were transfected with PB-TO-hNGN2 vector (gift from M. Ward, NIH, Maryland) in a 1:2 ratio (transposase:vector) using Lipofectamine Stem (ThermoFisher). After 72 hours, transfected iPSCs were selected for 48 hours with 0.5 µg/mL puromycin (Takara). Induction into neuronal fate with doxycycline and cryopreservation of pre-differentiated neurons was performed as described above (“i³Neuron differentiation”).

Culture and transfection of iPSC-derived neurons

Cryo-preserved, pre-differentiated iNeurons (i³Neurons or Piggybac-delivered NGN2 neurons) were thawed and plated on live-imaging dishes (MatTek) coated with poly-L-ornithine at a density of 300,000 neurons per dish. For each experimental condition, cells from at least two different batches of induction were used over three or more independent experimental cultures. iPSC-derived neurons were cultured in BrainPhys Neuronal Media (StemCell) supplemented with 2% B-27 (GIBCO), 10 ng/mL BDNF (PeproTech), 10 ng/mL NT-3 (PeproTech), and 1 µg/mL laminin (Corning). 40% of the media was replaced with fresh media twice per week. For Piggybac-delivered NGN2 neurons, 10 µM 5-Fluoro-2'-deoxyuridine and 10 µM uridine were included at the time of plating to prevent survival of mitotic cells. These drugs were removed 24 hours after plating. Live imaging experiments were performed 21 days after thawing pre-

differentiated iPSC-derived neurons (DIV21). On DIV18, iPSC-derived neurons were transfected with Lipofectamine Stem (ThermoFisher) and 1-2.5 µg total plasmid DNA.

METHOD DETAILS

Plasmids

Plasmids used include PGK EGFP-LC3 (subcloned from PGK mCherry-LC3B, gift from Michael Ward, National Institutes of Health, Maryland), PGK 4xMito-mEmerald (subcloned from 4xMito-mScarlet-I, Addgene plasmid #98818), PGK ARF6^{Q67L}-CFP (subcloned from CMV ARF6^{Q67L}-CFP, Addgene plasmid ##11387), PGK CFP (subcloned from CMV ARF6^{Q67L}-CFP, Addgene plasmid ##11387), CMV mScarlet-LC3B (subcloned from EGFP-LC3B, gift from T. Yoshimori, Osaka University, Japan, with mScarlet from Addgene plasmid #85054), CMV EGFP-PPM1H-WT (#DU62939, MRC PPU reagents and services, University of Dundee, Scotland), CMV EGFP-PPM1H-H153D (subcloned from pLVX HA PPM1H H153D #DU66215, acquired from MRC PPU reagents and services, University of Dundee, Scotland), CMV FLAG-LRRK2-R1441G (#DU13077, MRC PPU reagents and services, University of Dundee, Scotland), PB-TO-hNGN2 (gift from iPSC Neurodegenerative Disease Initiative (iNDI) & Michael Ward, Addgene plasmid #172115), and piggyBacTM transposase vector (available from Transposagen).

Generation of PPM1H KO iPSCs

For CRISPR/Cas9 gene editing, KOLF2.1J iPSCs were cultured on Matrigel coated plates in mTeSR medium (StemCell). 800,000 iPSCs were individualized with Accutase and plated onto one well of a Matrigel-coated 6-well plate. iPSCs were then transfected with synthetic sgRNA (Synthego, Gene knockout kit v2 – PPM1H), recombinant Alt-R HiFi Cas9 Nuclease V3 (IDT), and a plasmid encoding for GFP using Lipofectamine Stem Transfection Reagent (ThermoFisher) following the manufacturers' instructions (12 µL of 1 µM HiFi Cas9 + 12 µL of 1 µM sgRNA in 76 µL OptiMEM combined with 4 µL Lipofectamine Stem in 100 µL OptiMEM). On the following day, iPSCs were split with Accutase and plated in 6 wells of a 6-well plate. 72 hours after transfection, iPSCs were sorted through FACS and 10,000 GFP⁺ cells were plated on a Matrigel-coated 10 cm dish. Cells were grown for 9 days, then individual colonies were picked. Successful editing was confirmed by Western blot. Karyotype analysis (Cell Line Genetics) demonstrated a normal karyotype of the clone used in this study.

Live-cell imaging and motility quantification

Primary mouse cortical neurons were imaged on DIV7 in low fluorescence Hibernate E medium (Brain Bits) supplemented with 2% B27 and 2 mM GlutaMAX. iNeurons were imaged on DIV21 in low fluorescence Hibernate A medium (Brain Bits) supplemented with 2% B27, 10 ng/mL BDNF and 10 ng/mL

NT-3. Neurons were imaged in an environmental chamber at 37°C. Recordings of mScarlet-LC3 vesicles in mouse cortical neurons as well as EGFP-LC3 vesicles and mitochondria in WT vs. LRRK2-R1441H iNeurons were acquired on a PerkinElmer UltraView Vox Spinning Disk Confocal system with a Nikon Eclipse Ti inverted microscope, using a Plan Apochromat 60x 1.40 NA oil immersion objective and a Hamamatsu EMCCD C9100-50 camera controlled by Volocity software. Following a scheduled microscope upgrade, the last replicate of the live imaging experiment investigating mitochondrial transport in *LRRK2*-p.R1441H KI iNeurons and all replicates of the experiment investigating the effect of ARF6^{Q67L}-CFP overexpression in *LRRK2*-p.R1441H iNeurons were instead performed using a Hamamatsu ORCA-Fusion C14440-20UP camera controlled by VisiView software. Experiments investigating EGFP-LC3 transport in PPM1H KO iNeurons were performed at the Live-Cell Imaging Facility of the Max Planck Institute for Multidisciplinary Sciences, Goettingen, on a Visitron CSU-W1 Spinning Disk Confocal system with a Nikon Ti2 inverted microscope using a Plan Apochromat 60x 1.40 NA oil immersion objective and a Prime BSI sCMOS camera controlled by VisiView software. Axons were identified based on morphological parameters (Boecker et al., 2020; Kaech and Banker, 2006). All time lapse recordings were acquired in the mid-axon (> 300 µm from the soma and > 100 µm from the distal axon terminal) at a frame rate of 1 frame/sec for 5 minutes.

Kymographs of axonal autophagosomes and mitochondria were generated using the Multiple Kymograph plugin (FIJI). Line width was set to 5 pixels. Tracks were traced manually using a custom MATLAB GUI (KymoSuite). Motile autophagosomes and mitochondria were scored as anterograde (net displacement >10 µm in the anterograde direction within the 5-minute time lapse duration), retrograde (net displacement >10 µm in the retrograde direction), or bi-directional (net displacement <10 µm in either direction but total displacement >10 µm). Autophagosomes and mitochondria were scored as stationary if net and total displacement were <10 µm. A pause was defined as a single or consecutive instantaneous velocity value of < 0.083 µm/sec. Bi-directional organelles were included in quantification of pause number, pause duration, directional reversals, and Δ run length, but stationary organelles were excluded. Quantification of the fraction of time paused included all (motile and stationary) autophagosomes. For quantification of Δ run length, the net run length of each vesicle was subtracted from its total run length (Figure S2B). All analyses were performed by a blinded investigator.

Figure legends contain the statistical test used and specific p values for each quantification. For directionality analysis for both AV and mitochondrial transport experiments, two-way ANOVA analysis with Sidak's test for multiple comparisons was performed using GraphPad Prism 9. For other transport parameters, RStudio version 2021.9.2.382 was used to perform either a linear mixed effects model (LME;

R package “nlme”) or a generalized linear mixed model (GLMM; R package “lme4”). The genotype (or, in MLI-2 experiments, the treatment condition) was treated as the fixed effect. The independent experiment/culture and the neuron being recorded from were treated as nested random effects, with the neuron nested within the experiment. Specific models used were chosen based on distribution of each dataset and diagnostic residual plots. In detail, the following models were used: for fraction of time paused, GLMM (binomial family, with the “weights” argument for total time); for pause number, GLMM (Poisson family); for pause duration, GLMM (gamma family, log link function); for reversals, GLMM (Poisson family); for Δ run length, GLMM (gamma family, log link function, with transformation to remove zero values with added constants); for mito density, LME; for mito length, LME. In situations where gamma family GLMMs failed to converge (Figures 1E, 2D, 3D, 4G, 6D, and 6F), adaptive Gauss-Hermite quadrature (nAGQ=0) was used instead of the default Laplace approximation (nAGQ=1). For all quantifications, at least three independent experiments were analyzed.

Immunoblotting

Neurons or MEFs were washed twice with ice cold PBS and lysed with RIPA buffer (50 mM Tris-HCl, 150 mM NaCl, 0.1% Triton X-100, 0.5% deoxycholate, 0.1% SDS, 2x Halt Protease and Phosphatase inhibitor, 2mg/mL microcystin-LR). Samples were centrifuged for 10 min at 17,000 g, and protein concentration of the supernatant was determined by BCA assay. Proteins were resolved on 8% (LRRK2) - 15% (PPM1H or RAB proteins) acrylamide gels. Proteins were transferred to Immobilon-FL PVDF membranes (Millipore) using a wet blot transfer system. Membranes were then stained for total protein using LI-COR Revert 700 Total Protein Stain. Following imaging of total protein stain, membranes were de-stained and blocked for 5 minutes with Bio-Rad EveryBlot blocking buffer. For PPM1H and pan-specific phosphothreonine RAB blots, membranes were incubated with primary antibody diluted in EveryBlot for 90 minutes at room temperature. For pT73 RAB10 and total RAB10 blots (Figure S3), membranes were incubated with primary antibody diluted in EveryBlot at 4°C overnight. After three washes with TBS (50 mM Tris-HCl [pH 7.4], 274 mM NaCl, 9 mM KCl) with 0.1% Tween-20, membranes were incubated with secondary antibodies diluted in EveryBlot with 0.01% SDS for 1 hr at RT. Following three more washes with TBS with 0.1% Tween-20, membranes were imaged using an Odyssey CLx Infrared Imaging System (LI-COR). Western blots were analyzed with Image Studio Software (LI-COR).

SUPPLEMENTAL VIDEO TITLES AND LEGENDS

Video S1. *LRRK2*-p.R1441H knock-in disrupts axonal AV transport in human iNeurons. Time lapse recording of axonal EGFP-LC3+ vesicles in WT and *LRRK2*-p.R1441H iNeurons. Arrowheads highlight AVs; arrowhead color matches the color of the kymograph traces shown in Figure 1A. Toward the left is retrograde.

Video S2. Cotransport of GPF-PPM1H and mScarlet-LC3 in *Lrrk2*-p.G2019S knock-in mouse cortical neurons. Time lapse recording of axonal GFP-PPM1H^{WT}+ and mScarlet-LC3+ vesicles in *Lrrk2*-p.G2019S mouse cortical neurons. Arrowheads highlight axonal AVs. Toward the left is retrograde.

Video S3. Overexpression of PPM1H^{WT} rescues AV transport in *Lrrk2*-p.G2019S knock-in mouse cortical neurons. Time lapse recording of axonal mScarlet-LC3+ vesicles in *Lrrk2*-p.G2019S mouse cortical neurons overexpressing GFP, GFP-PPM1H^{WT}, or GFP-PPM1H^{H153D}. Arrowheads highlight AVs; arrowhead color matches the color of the kymograph traces shown in Figure 2A. Toward the left is retrograde.

Video S4. Knock-out of PPM1H causes disruption of axonal AV transport in human iNeurons. Time lapse recording of axonal EGFP-LC3+ vesicles in WT and PPM1H KO iNeurons. Arrowheads highlight AVs; arrowhead color matches the color of the kymograph traces shown in Figure 3A. Toward the left is retrograde.

Video S5. *LRRK2*-p.R1441H does not disrupt axonal mitochondria transport in human iNeurons. Time lapse recording of axonal mitochondria labeled by Mito-mEmerald in WT and p.R1441H KI iNeurons. Arrowheads highlight mitochondria; arrowhead color matches the color of the kymograph traces shown in Figure 4A. Toward the left is retrograde.

Video S6. Overexpression of ARF6^{Q67L} ameliorates AV transport deficits in *LRRK2*-p.R1441H KI iNeurons. Time lapse recording of axonal EGFP-LC3+ vesicles in *LRRK2*-p.R1441H iNeurons overexpressing CFP or ARF6^{Q67L}-CFP. Arrowheads highlight AVs; arrowhead color matches the color of the kymograph traces shown in Figure 5A. Toward the left is retrograde.

REFERENCES

- Berndsen, K., Lis, P., Yeshaw, W.M., Wawro, P.S., Nirujogi, R.S., Wightman, M., Macartney, T., Dorward, M., Knebel, A., Tonelli, F., et al. (2019). PPM1H phosphatase counteracts LRRK2 signaling by selectively dephosphorylating Rab proteins. *Elife* 8, 1–37.
- Bieri, G., Brahic, M., Bousset, L., Couthouis, J., Kramer, N.J., Ma, R., Nakayama, L., Monbureau, M., Defensor, E., Schüle, B., et al. (2019). LRRK2 modifies α -syn pathology and spread in mouse models and human neurons. *Acta Neuropathol.* 137, 961–980.
- Boecker, C.A., and Holzbaur, E.L.F. (2021). Hyperactive LRRK2 kinase impairs the trafficking of axonal autophagosomes. *Autophagy* 00, 1–3.
- Boecker, C.A., Olenick, M.A., Gallagher, E.R., Ward, M.E., and Holzbaur, E.L.F. (2020). ToolBox: Live Imaging of intracellular organelle transport in induced pluripotent stem cell-derived neurons. *Traffic* 21, 138–155.
- Boecker, C.A., Goldsmith, J., Dou, D., Cajka, G.G., and Holzbaur, E.L.F. (2021). Increased LRRK2 kinase activity alters neuronal autophagy by disrupting the axonal transport of autophagosomes. *Curr. Biol.* 1–15.
- Bonet-Ponce, L., Beilina, A., Williamson, C.D., Lindberg, E., Kluss, J.H., Saez-Atienzar, S., Landeck, N., Kumaran, R., Mamais, A., Bleck, C.K.E., et al. (2020). LRRK2 mediates tubulation and vesicle sorting from lysosomes. *Sci. Adv.* 6, 1–16.
- Bose, A., and Beal, M.F. (2016). Mitochondrial dysfunction in Parkinson’s disease. *J. Neurochem.* 139, 216–231.
- Cason, S.E., and Holzbaur, E.L.F. (2022). Selective motor activation in organelle transport along axons. *Nat. Rev. Mol. Cell Biol.* 0123456789.
- Cason, S.E., Carman, P.J., Van Duyne, C., Goldsmith, J., Dominguez, R., and Holzbaur, E.L.F. (2021). Sequential dynein effectors regulate axonal autophagosome motility in a maturation-dependent pathway. *J. Cell Biol.* 220.
- Cason, S.E., Mogre, S.S., Holzbaur, E.L.F., and Koslover, E.F. (2022). Spatiotemporal analysis of axonal autophagosome-lysosome dynamics reveals limited fusion events and slow maturation. *Mol. Biol. Cell* 3, 58–66.
- Cheng, X.T., Zhou, B., Lin, M.Y., Cai, Q., and Sheng, Z.H. (2015). Axonal autophagosomes recruit dynein for retrograde transport through fusion with late endosomes. *J. Cell Biol.* 209, 377–386.
- Dhekne, H.S., Yanatori, I., Gomez, R.C., Tonelli, F., Steger, M., Alessi, D.R., Diez, F., Schu, B., and Pfeffer, S.R. (2018). A pathway for Parkinson’s Disease LRRK2 kinase to block primary cilia and Sonic hedgehog signaling in the brain. 1–26.
- Domingo, A., and Klein, C. (2018). Genetics of Parkinson disease (Elsevier B.V.).
- Farfel-Becker, T., Roney, J.C., Cheng, X., Li, S., Cuddy, S.R., and Sheng, Z. (2019). Neuronal Soma-Derived Degradative Lysosomes Are Continuously Delivered to Distal Axons to Maintain Local Degradation Capacity. *Cell Rep.* 28, 51-64.e4.
- Fell, M.J., Mirescu, C., Basu, K., Cheewatrakoolpong, B., DeMong, D.E., Ellis, J.M., Hyde, L.A., Lin, Y., Markgraf, C.G., Mei, H., et al. (2015). MLI-2, a Potent, Selective, and Centrally Active Compound for Exploring the Therapeutic Potential and Safety of LRRK2 Kinase Inhibition. *J. Pharmacol. Exp. Ther.*

355, 397–409.

Fenton, A.R., Jongens, T.A., and Holzbaur, E.L.F. (2021). Mitochondrial dynamics: Shaping and remodeling an organelle network. *Curr. Opin. Cell Biol.* 68, 28–36.

Fernandopulle, M.S., Prestil, R., Grunseich, C., Wang, C., Gan, L., and Ward, M.E. (2018). Transcription Factor-Mediated Differentiation of Human iPSCs into Neurons. *Curr. Protoc. Cell Biol.* 79, e51.

Fonseca-Ornelas, L., Stricker, J.M.S., Soriano-Cruz, S., Weykopf, B., Dettmer, U., Muratore, C.R., Scherzer, C.R., and Selkoe, D.J. (2022). Parkinson-causing mutations in LRRK2 impair the physiological tetramerization of endogenous α -synuclein in human neurons. *Npj Park. Dis.* 8, 1–10.

Friedman, L.G., Lachenmayer, M.L., Wang, J., He, L., Poulouse, S.M., Komatsu, M., Holstein, G.R., and Yue, Z. (2012). Disrupted Autophagy Leads to Dopaminergic Axon and Dendrite Degeneration and Promotes Presynaptic Accumulation of α -Synuclein and LRRK2 in the Brain. *J. Neurosci.* 32, 7585–7593.

Fu, M. meng, and Holzbaur, E.L.F. (2014). Integrated regulation of motor-driven organelle transport by scaffolding proteins. *Trends Cell Biol.* 24, 564–574.

Fu, M., Nirschl, J.J., and Holzbaur, E.L.F. (2014). LC3 Binding to the Scaffolding Protein JIP1 Regulates Processive Dynein-Driven Transport of Autophagosomes. *Dev. Cell* 29, 577–590.

Goldsmith, J., Ordureau, A., Harper, J.W., and Holzbaur, E.L.F. (2022). Brain-derived autophagosome profiling reveals the engulfment of nucleoid-enriched mitochondrial fragments by basal autophagy in neurons. *Neuron* 1–10.

Guedes-Dias, P., Nirschl, J.J., Abreu, N., Tokito, M.K., Janke, C., Magiera, M.M., and Holzbaur, E.L.F. (2019). Kinesin-3 Responds to Local Microtubule Dynamics to Target Synaptic Cargo Delivery to the Presynapse. *Curr. Biol.* 29, 268-282.e8.

Haugarvoll, K., Rademakers, R., Kachergus, J.M., Nuytemans, K., Ross, O.A., Gibson, J.M., Tan, E.-K., Gaig, C., Tolosa, E., Goldwurm, S., et al. (2008). Lrrk2 R1441C parkinsonism is clinically similar to sporadic Parkinson disease. *Neurology* 70, 1456–1460.

Healy, D.G., Falchi, M., O’Sullivan, S.S., Bonifati, V., Durr, A., Bressman, S., Brice, A., Aasly, J., Zabetian, C.P., Goldwurm, S., et al. (2008). Phenotype, genotype, and worldwide genetic penetrance of LRRK2-associated Parkinson’s disease: a case-control study. *Lancet Neurol.* 7, 583–590.

Ho, P.W.-L., Chang, E.E., Leung, C.-T., Liu, H., Malki, Y., Pang, S.Y., Choi, Z.Y., Liang, Y., Lai, W.S., Ruan, Y., et al. (2022). Long-term inhibition of mutant LRRK2 hyper-kinase activity reduced mouse brain α -synuclein oligomers without adverse effects. *Npj Park. Dis.* 8, 115.

Hsieh, C.-H., Shaltouki, A., Gonzalez, A.E., Bettencourt da Cruz, A., Burbulla, L.F., St. Lawrence, E., Schüle, B., Krainc, D., Palmer, T.D., and Wang, X. (2016). Functional Impairment in Miro Degradation and Mitophagy Is a Shared Feature in Familial and Sporadic Parkinson’s Disease. *Cell Stem Cell* 19, 709–724.

Kaech, S., and Banker, G. (2006). Culturing hippocampal neurons. *Nat. Protoc.* 1, 2406–2415.

Kalogeropoulou, A.F., Purlyte, E., Tonelli, F., Lange, S.M., Wightman, M., Prescott, A.R., Padmanabhan, S., Sammler, E., and Alessi, D.R. (2022). Impact of 100 LRRK2 variants linked to Parkinson’s Disease on kinase activity and microtubule binding. *Biochem. J.*

Khan, S.S., Sobu, Y., Dhekne, H.S., Tonelli, F., Berndsen, K., Alessi, D.R., and Pfeffer, S.R. (2021). Pathogenic LRRK2 control of primary cilia and Hedgehog signaling in neurons and astrocytes of mouse

brain. *Elife* 10, 1–25.

Klein, C., and Westenberg, A. (2012). Genetics of Parkinson's Disease. *Cold Spring Harb. Perspect. Med.* 2, a008888–a008888.

Kluss, J.H., Bonet-Ponce, L., Lewis, P.A., and Cookson, M.R. (2022). Directing LRRK2 to membranes of the endolysosomal pathway triggers RAB phosphorylation and JIP4 recruitment. *Neurobiol. Dis.* 170, 105769.

MacIsaac, S., Quevedo Melo, T., Zhang, Y., Volta, M., Farrer, M.J., and Milnerwood, A.J. (2020). Neuron-autonomous susceptibility to induced synuclein aggregation is exacerbated by endogenous Lrrk2 mutations and ameliorated by Lrrk2 genetic knock-out. *Brain Commun.* 2.

Maday, S., and Holzbaur, E.L.F. (2014). Autophagosome biogenesis in primary neurons follows an ordered and spatially regulated pathway. *Dev. Cell* 30, 71–85.

Maday, S., Wallace, K.E., and Holzbaur, E.L.F. (2012). Autophagosomes initiate distally and mature during transport toward the cell soma in primary neurons. *J. Cell Biol.* 196, 407–417.

Montagnac, G., Sibarita, J.B., Loubéry, S., Daviet, L., Romao, M., Raposo, G., and Chavrier, P. (2009). ARF6 Interacts with JIP4 to Control a Motor Switch Mechanism Regulating Endosome Traffic in Cytokinesis. *Curr. Biol.* 19, 184–195.

Neisch, A.L., Neufeld, T.P., and Hays, T.S. (2017). A STRIPAK complex mediates axonal transport of autophagosomes and dense core vesicles through PP2A regulation. *J. Cell Biol.* 216, 441–461.

Pantazis, C.B., Yang, A., Lara, E., McDonough, J.A., Blauwendraat, C., Peng, L., Oguro, H., Zou, J., Sebesta, D., Pratt, G., et al. (2022). A reference induced pluripotent stem cell line for large-scale collaborative studies. *BioRxiv* 2021.12.15.472643.

Pfeffer, S.R. (2022). LRRK2 phosphorylation of Rab GTPases in Parkinson's disease. *FEBS Lett.* 1–15.

Ramos, D.M., Skarnes, W.C., Singleton, A.B., Cookson, M.R., and Ward, M.E. (2021). Tackling neurodegenerative diseases with genomic engineering: A new stem cell initiative from the NIH. *Neuron* 109, 1080–1083.

Riley, J.S., and Tait, S.W. (2020). Mitochondrial DNA in inflammation and immunity. *EMBO Rep.* 21, 1–17.

Ruiz-Martínez, J., Gorostidi, A., Ibañez, B., Alzualde, A., Otaegui, D., Moreno, F., De Munain, A.L., Bergareche, A., Gómez-Esteban, J.C., and Massó, J.F.M. (2010). Penetrance in Parkinson's disease related to the LRRK2 R1441G mutation in the Basque country (Spain). *Mov. Disord.* 25, 2340–2345.

Schapansky, J., Khasnavis, S., DeAndrade, M.P., Nardozzi, J.D., Falkson, S.R., Boyd, J.D., Sanderson, J.B., Bartels, T., Melrose, H.L., and LaVoie, M.J. (2018). Familial knockin mutation of LRRK2 causes lysosomal dysfunction and accumulation of endogenous insoluble α -synuclein in neurons. *Neurobiol. Dis.* 111, 26–35.

Stavoe, A.K.H., Hill, S.E., Hall, D.H., and Colón-Ramos, D.A. (2016). KIF1A/UNC-104 Transports ATG-9 to Regulate Neurodevelopment and Autophagy at Synapses. *Dev. Cell* 38, 171–185.

Steger, M., Tonelli, F., Ito, G., Davies, P., Trost, M., Vetter, M., Wachter, S., Lorentzen, E., Duddy, G., Wilson, S., et al. (2016). Phosphoproteomics reveals that Parkinson's disease kinase LRRK2 regulates a subset of Rab GTPases. *Elife* 5, 1–28.

- Vogiatzi, T., Xilouri, M., Vekrellis, K., and Stefanis, L. (2008). Wild type α -synuclein is degraded by chaperone-mediated autophagy and macroautophagy in neuronal cells. *J. Biol. Chem.* 283, 23542–23556.
- Volpicelli-Daley, L.A., Abdelmotilib, H., Liu, Z., Stoyka, L., Daher, J.P.L., Milnerwood, A.J., Unni, V.K., Hirst, W.D., Yue, Z., Zhao, H.T., et al. (2016). G2019S-LRRK2 expression augments α -synuclein sequestration into inclusions in neurons. *J. Neurosci.* 36, 7415–7427.
- Wallings, R.L., and Tansey, M.G. (2019). LRRK2 regulation of immune-pathways and inflammatory disease. *Biochem. Soc. Trans.* 47, 1581–1595.
- Wang, C., Ward, M.E., Chen, R., Liu, K., Tracy, T.E., Chen, X., Xie, M., Sohn, P.D., Ludwig, C., Meyer-Franke, A., et al. (2017). Scalable Production of iPSC-Derived Human Neurons to Identify Tau-Lowering Compounds by High-Content Screening. *Stem Cell Reports* 9, 1221–1233.
- Waschbüsch, D., Purlyte, E., Pal, P., McGrath, E., Alessi, D.R., and Khan, A.R. (2020). Structural Basis for Rab8a Recruitment of RILPL2 via LRRK2 Phosphorylation of Switch 2. *Structure* 28, 406-417.e6.
- Wong, Y.C., and Holzbaur, E.L.F. (2014). The Regulation of Autophagosome Dynamics by Huntingtin and HAP1 Is Disrupted by Expression of Mutant Huntingtin, Leading to Defective Cargo Degradation. *J. Neurosci.* 34, 1293–1305.
- Wu, C.X., Liao, J., Park, Y., Reed, X., Engel, V.A., Hoang, N.C., Takagi, Y., Johnson, S.M., Wang, M., Federici, M., et al. (2019). Parkinson’s disease-associated mutations in the GTPase domain of LRRK2 impair its nucleotide-dependent conformational dynamics. *J. Biol. Chem.* 294, 5907–5913.